

Tomographic-spectral approach for dark matter detection in the cross-correlation between cosmic shear and diffuse gamma-ray emission

S. Camera,^a M. Fornasa,^b N. Fornengo^{c,d} and M. Regis^{c,d}

^aCENTRA, Instituto Superior Técnico, Universidade de Lisboa,
Avenida Rovisco Pais 1, 1049-001 Lisboa, Portugal

^bSchool of Physics and Astronomy, University of Nottingham,
University Campus, Nottingham NG7 2RD, UK

^cDipartimento di Fisica, Università di Torino,
Via P. Giuria 1, 10125 Torino, Italy

^dINFN, Sezione di Torino,
Via P. Giuria 1, 10125 Torino, Italy

E-mail: stefano.camera@tecnico.ulisboa.pt, fornasam@gmail.com,
fornengo@to.infn.it, regis@to.infn.it

Abstract. We recently proposed to cross-correlate the diffuse γ -ray emission with the gravitational lensing signal of cosmic shear. This represents a novel and promising strategy to search for annihilating or decaying dark matter (DM) candidates. In the present work, we demonstrate the potential of a tomographic-spectral approach: measuring the cross-correlation in separate bins of redshift *and* energy significantly improves the sensitivity to a DM signal. Indeed, the power of the proposed technique stems from the capability of simultaneously exploiting the different redshift scaling of astrophysical and DM components, their different energy spectra and their different angular shapes. The sensitivity to a particle DM signal is extremely promising even in the case the γ -ray emission induced by DM is a subdominant component in the isotropic γ -ray background. We quantify the prospects of detecting DM by cross-correlating the γ -ray emission from the Fermi large area telescope (LAT) with the cosmic shear measured by the Dark Energy Survey, using data sets that will be available in the near future. Under the hypothesis of a significant (but realistic) subhalo boost, such a measurement can deliver a 5σ detection of DM, if the DM particle has a mass lighter than 300 GeV and thermal annihilation rate. Data from the European Space Agency *Euclid* satellite (launch planned for 2020) will be even more informative: if used to reconstruct the properties of the DM particle, the cross-correlation of *Euclid* and Fermi-LAT will allow for a measurement of the DM mass within a factor of 1.5–2, even for moderate subhalo boosts, assuming the DM mass around 100 GeV and a thermal annihilation rate.

Keywords: dark matter theory, weak gravitational lensing, gamma-ray experiments.

Contents

1	Introduction	1
2	Intensity of γ-ray emission and cosmic shear	4
2.1	Dark matter	4
2.1.1	Annihilating dark matter	4
2.1.2	Decaying dark matter	6
2.2	Astrophysical sources	6
2.2.1	Blazars	8
2.2.2	Misaligned AGNs	8
2.2.3	Star-forming galaxies	8
2.3	Cosmic shear	9
3	Auto- and cross-correlation angular power spectra	9
3.1	Angular power spectrum of γ -ray emission	10
3.1.1	Dark matter	10
3.1.2	Astrophysical sources	11
3.2	Cross-correlation of cosmic shear and γ -ray emission	14
3.2.1	Dark matter	14
3.2.2	Blazars	15
3.2.3	Misaligned AGNs	16
3.2.4	Star-forming galaxies	17
4	The tomographic-spectral approach	20
4.1	Survey specifications	21
5	Analysis technique	24
5.1	Fisher matrix fundamentals	24
6	Results	26
6.1	Detection reach	26
6.2	Parameter estimation	30
7	Conclusions	35
A	The $M(\mathcal{L})$ relation for misaligned Active Galactic Nuclei	38
B	The $M(\mathcal{L})$ relation for star-forming galaxies	40

1 Introduction

A tremendous experimental effort is underway with the goal of delivering the much awaited first non-gravitational detection of dark matter (DM). Indeed, very little is known about its nature despite its huge abundance [1], and the community is eager for new and innovative ideas able to broaden our current understanding of DM.

In Ref. [2] (Paper I), we demonstrate, for the first time, how distinctive signatures of DM can be detected in the cross-correlation between the unresolved component of the so-called extra-galactic γ -ray background (EGB) and the weak lensing effect of cosmic shear—an unbiased tracer of the DM distribution in the Universe.

The EGB is the residual emission remaining after the contribution of the resolved γ -ray sources (both point-like and extended) and of the Galactic foreground (due to the interaction of cosmic rays with the Galactic interstellar medium) are subtracted from the total γ -ray radiation. The latest measurement of the EGB was performed by the Fermi-LAT satellite over the energy range between 200 MeV and 800 GeV [3]. Unresolved astrophysical sources like blazars [4–10], misaligned Active Galactic Nuclei (mAGNs) [9, 11] and star-forming galaxies (SFGs) [12–14] are guaranteed components to the EGB, but γ rays produced by DM annihilations or decays in Galactic or extra-galactic (sub)haloes may also play a relevant rôle (see Refs [15–24], amongst others).

In Ref. [25], Fermi-LAT measured the auto-correlation angular power spectrum (APS), reporting a Poisson-like signal with a significance ranging from 7.1σ (between 2 and 5 GeV) to 2.4σ (between 10 and 50 GeV). The measurement of the intensity and of the auto-correlation angular power spectrum (APS) of the EGB can be used to reconstruct its composition and constrain the DM-induced component (see e.g. Refs [24, 26, 27]). The picture that arises suggests that unresolved blazars can explain the whole auto-correlation signal [8, 26] by themselves alone, whereas they are responsible for only $\lesssim 25\%$ of the EGB intensity [7, 9, 10]. Thus, other contributions are needed to reproduce the EGB intensity energy spectrum. At the same time, such contributions have to be more isotropic than blazars, in order not to contribute much to the auto-correlation APS.

Cross-correlating the EGB with other observables can provide additional and complementary information (some possibilities are summarised in Ref. [28]). In Paper I, we demonstrated that the cross-correlation with the cosmic shear is particularly compelling since, in this case, the contribution of unresolved blazars is subdominant and the signal is therefore more sensitive to components that would be difficult to isolate by the study of the EGB intensity or of the auto-correlation APS.

The cosmic shear is a measure of the shape distortions of distant galaxies images due to the weak gravitational lensing produced by the distribution of intervening matter between the galaxies and the observer [29–32]. It is expected to cross-correlate with the EGB since the same concentrations of matter generating the photon path distortions are also responsible for the γ -ray emission, either because the annihilations (or decays) of DM produce γ -ray radiation or because DM structures host astrophysical γ -ray emitters.

In Paper I, we compute the cross-correlation APS between the cosmic shear expected from the Dark Energy Survey (DES) [33] or the *Euclid* satellite [34, 35]¹ and the γ -ray emission produced by different classes of sources, namely DM extra-galactic (sub)haloes, blazars and SFGs. The results are extremely promising and they suggest that DM haloes can be the class of sources associated with the largest cross-correlation (both in the case of annihilating and decaying DM) and that, with a statistics in γ rays typical of 5 years of Fermi-LAT data, it will be possible to detect DM-induced signatures in the cross-correlation of the EGB and the cosmic shear.

Since then, Ref. [36] measured the 2-point correlation function of the Fermi-LAT data gathered until January 2014 with the cosmic shear detected by the Canada-France-Hawaii

¹<http://www.euclid-ec.org/>

Telescope Lensing Survey (CFTHLenS) [37]. The measurement was consistent with no signal and the null detection was used to derive constraints on the DM annihilation cross section. Over a certain range of masses and for specific annihilation channels, the upper limits from Ref. [36] can exclude annihilation cross sections smaller than the thermal value of $3 \times 10^{-26} \text{ cm}^3 \text{ s}^{-1}$, depending on the clustering and astrophysical scenarios adopted. This fact additionally proves the potential of such a technique for the indirect detection of DM.

Along the same line, the cross-correlation of the EGB with other large scale structure tracers such as galaxies is also a potentially very valuable technique to infer the EGB composition and to possibly disentangle a DM contribution [28, 38–40].

Recently, Ref. [41] found the first evidence of a cross-correlation between weak lensing of the cosmic microwave background (CMB) and the γ -ray sky. Since the kernel of the CMB lensing peaks at a redshift $z \sim 2$, this observable is more suited to constraint astrophysical contributions to the EGB. Indeed, their emission mostly comes from intermediate z , while the DM-induced signal peaks at lower redshift, as we will discuss later.

In the present work, we investigate the importance of a combined tomographic and spectral approach for the study of the cross-correlation between cosmic shear and γ -ray emission. Moreover, with respect to Paper I, we complement our model of the EGB by including the contribution of unresolved mAGNs. Such a component, together with unresolved SFGs, is associated to a quite large cross-correlation APS. Those two contributions, which are most probably responsible for the majority of the EGB intensity, represent the most relevant astrophysical backgrounds when looking for DM signatures in the cross-correlation. However, the abundance of those classes of sources as a function of redshift is quite different from the case of DM. Tomography exploits this fact, isolating the cross-correlation APS in different redshift bins and studying how the APS changes as a function of z . This is expected to significantly boost the capability of the cross-correlation APS to dissect the EGB into components and to discriminate DM from astrophysical contributions.

Here, we also investigate how performing the analysis into different bins in energy can further enhance the discriminatory power between astrophysical sources (typically characterised by power-law spectra) and the emission expected from DM. As we will show below, the spectral analysis is also crucial for inferring the DM microscopic properties, allowing us to lift the degeneracy between its mass and annihilation/decay rate—both entering the computation of the cross-correlation signal.

Our final aim is to fully exploit the complementary information coming from the angular, redshift, and spectral distribution of the extragalactic signal.

The analysis will focus on the expected weak lensing observations from DES (whose data and maps will be available in the next years) and *Euclid*. The latter is an experiment that will start taking data only in 2020 but with a highly improved sensitivity to the cosmic shear signal. That is why *Euclid* will have excellent prospects of detecting the signal we are looking for. For what concerns γ rays, we will first consider 5 nominal years (i.e. after cuts) of data from the Fermi-LAT telescope. This represents approximately the amount of data available at present. For future prospects, we will also consider 10 nominal years of Fermi-LAT data (available approximately at the end of expected lifetime of the telescope), and a possible near-future instrument similar to Fermi-LAT but with improved capabilities.

In the following, we shall compute the sensitivity to a DM detection through the tomographic measurement of the cross-correlation APS of the EGB and gravitational lensing. Furthermore, we shall estimate the precision with which it is possible to determine DM properties by such a measurement, like its mass and its annihilation or decay rates. This will

be achieved by means of a statistical analysis based on the method of the Fisher matrix. This technique is extremely flexible and it allows for a systematic scrutiny of the main uncertainties pertaining our modelling of the DM distribution and of the astrophysical sources contributing to the EGB.

The paper is organised as follows: in Sec. 2 we summarise the details of the computation of the mean (all-sky averaged) γ -ray emission associated with the classes of sources considered, as well as of the cosmic shear signal. In Sec. 3 we derive the γ -ray auto-correlation APS of those sources, as well as their cross-correlation APS with cosmic shear. We shall take special care in emphasising the assumptions made and in estimating their impact on our results. Sec. 4 introduces the tomographic and spectral technique, whilst the Fisher analysis will be described in Sec. 5. In Sec. 6 we derive the forecasts for DM detection/bounds. Conclusions are drawn in Sec. 7.

Throughout the paper we assume a flat Λ CDM cosmology with cosmological parameters as derived by the Planck satellite [1]. We also assume the standard weakly interacting massive particle (WIMP) paradigm in which the DM particle has a mass m_{DM} of the order of GeV-TeV and its interactions are of the weak scale.

2 Intensity of γ -ray emission and cosmic shear

In this section, we introduce the formalism adopted when describing the γ -ray emission produced by different classes of sources, as well as the intensity of the cosmic shear signal. In this common framework, an observable $X(\chi, \hat{\mathbf{n}})$ can be written as

$$\mathcal{I}^X(\hat{\mathbf{n}}) = \int d\chi X(\chi, \hat{\mathbf{n}}) = \int d\chi g_X(\chi, \hat{\mathbf{n}}) \widetilde{W}^X(\chi). \quad (2.1)$$

Depending on the observable considered, $\mathcal{I}^X(\hat{\mathbf{n}})$ indicates the γ -ray emission expected from a given class of sources or the intensity of the shear signal from the direction $\hat{\mathbf{n}}$ in the sky. Here, $\chi = \chi(z)$ is the comoving distance at redshift z and, for a flat Universe, $d\chi = c/H dz$ being c the speed of light and $H(z)$ the Hubble rate. The observable $X(\chi, \hat{\mathbf{n}})$ is seeded by the source field $g_X(\chi, \hat{\mathbf{n}})$, which encodes the dependence on the line-of-sight direction, $\hat{\mathbf{n}}$. We define the window function $W^X(\chi)$ (also called weight or selection function) as $W^X(\chi) \equiv \langle X \rangle(\chi) = \langle g_X \rangle(\chi) \widetilde{W}^X(\chi)$, where $\langle \cdot \rangle$ stands for sky average. The mean intensity $\langle \mathcal{I}^X \rangle$ can be then simply written as the integral of the window function, viz.

$$\langle \mathcal{I}^X \rangle = \int d\chi W^X(\chi). \quad (2.2)$$

In the following, we shall derive the window functions for the γ -ray emission from different classes of sources (Secs. from 2.1.1 to 2.2.2), as well as the window function for the cosmic shear (Sec. 2.3).

2.1 Dark matter

2.1.1 Annihilating dark matter

The γ rays produced by DM annihilations in (sub)haloes ($X = \gamma_{a\text{DM}}$) trace the DM density squared ρ_{DM}^2 , so that $g_{\gamma_{a\text{DM}}}(\chi, \hat{\mathbf{n}}) = \rho_{\text{DM}}^2(\chi, \hat{\mathbf{n}})$. The window function is

$$W^{\gamma_{a\text{DM}}}(\chi) = \frac{(\Omega_{\text{DM}} \rho_c)^2}{4\pi} \frac{\langle \sigma_a v \rangle}{2m_{\text{DM}}^2} [1 + z(\chi)]^3 \Delta^2(\chi) \int_{\Delta E_\gamma} dE_\gamma \frac{dN_a}{dE_\gamma} [E_\gamma(\chi)] e^{-\tau[\chi, E_\gamma(\chi)]}, \quad (2.3)$$

where Ω_{DM} is the cosmological abundance of DM, ρ_c is the critical density of the Universe and $z(\chi)$ is the redshift corresponding to the comoving distance χ . dN_a/dE_γ indicates the number of photons produced per annihilation and its dependence upon the energy determines the γ -ray spectrum, whilst $\langle\sigma_a v\rangle$ denotes the velocity-averaged annihilation rate, assumed to be the same in all haloes.

Different mechanisms of γ -ray production can contribute to dN_a/dE_γ . At the energies of interest for this paper (i.e. from a few GeV to a few hundreds of GeV) primary production is probably the most important. In this case, γ rays are either produced directly in the annihilations of the two DM particles (and therefore the photon yield is a monochromatic line) or are generated by hadronisation or radiative emission of the particles generated in the annihilations (such as quarks, leptons, gauge or Higgs bosons). Robust predictions can be obtained for dN_a/dE_γ , based on the results of events generators like PYTHIA [42], which is used in the present work. Photon yields originated from the hadronisation of quarks or gauge bosons share a quite common spectral shape, with a cut-off at an energy equal to m_{DM} . Hadronisations of τ leptons are associated to hard spectra. Possible bumps, localised close to the cut-off, may be possible due to final-state radiation or internal bremsstrahlung, whenever the annihilation has charged final states. Hence, the photon yield in Eq. (2.3) is integrated in an energy window ΔE_γ , which is established according to detector resolution and required statistics. The factor $\exp\{-\tau[\chi, E_\gamma(\chi)]\}$ accounts for the absorption due to the extra-galactic background light and we model τ as in Ref. [43]. Radiative emissions too (most notably, inverse Compton scattering) can contribute to the total DM-induced γ -ray production. However, for the sake of simplicity, since secondary emissions are more model-dependent than the prompt emission considered here—and they typically affect predictions only for multi-TeV DM annihilating into light leptons—they will be neglected here.

The last quantity in Eq. (2.3) is the so-called clumping factor $\Delta^2(\chi)$. It measures how much the γ -ray flux increases due to the clumpiness of the DM distribution. In the case of an annihilating DM particle, it reads

$$\Delta^2(\chi) \equiv \frac{\langle\rho_{\text{DM}}^2\rangle}{\bar{\rho}_{\text{DM}}^2} = \int_{M_{\text{min}}}^{M_{\text{max}}} dM \frac{dn}{dM} \int d^3\mathbf{x} \frac{\rho_h^2(\mathbf{x}|M, \chi)}{\bar{\rho}_{\text{DM}}^2}. \quad (2.4)$$

Eq. (2.4) shows that the computation of the clumping factor involves integrating the halo number density dn/dM , above the so-called minimal halo mass M_{min} multiplied by the total number of annihilations produced in the generic haloes of mass M at distance χ with density profile $\rho_h(\mathbf{x}|M, \chi)$. The exact value of M_{min} is unknown and it depends on the free-streaming length of the DM particle, with reasonable values ranging between 10^{-12} and $10^{-3}M_\odot$ [44, 45]. We consider a reference value of $10^{-6}M_\odot$, but we also report our results for a much more conservative value of 10^7M_\odot . This represents the smallest mass scale for which we have an indirect evidence of DM haloes from the study of the dynamics of stars in the dwarf spheroidal galaxies of the Milky Way. The case with $M_{\text{min}} = 10^7M_\odot$ represents one of the three benchmark descriptions of DM distribution that will be considered in the following; we refer to this as the ‘no substructures’ (NS) scenario, as no contribution from subhaloes are considered (see later). The maximal halo mass M_{max} will always be set to $10^{18}M_\odot$ and its value has only a minor impact on the results.

Many quantities in Eq. (2.4) can be derived from N -body simulations: we take the halo mass function from Ref. [46] and we assume that the haloes are characterised by the so-called Navarro-Frenk-White (NFW) universal density profile [47]. The profile is completely determined by the total mass of the halo and by its size. We express the latter in terms of the

concentration parameter $c(M)$, taken as a function of the halo mass M from Ref. [48]. Even though N -body simulations provide valuable information for massive DM haloes, they unfortunately do not cover the mass range considered in Eq. (2.4). Below their mass resolution our knowledge is very scarce and one has to resort to debatable assumptions. In the following sections we shall assume that haloes with a mass below $10^{10} M_\odot$ are still well described by a NFW profile with a mass function from Ref. [46], but we adopt the $c(M)$ relation presented in Ref. [49], renormalised so that it gives the same concentration as the model from Ref. [48] at $10^{10} M_\odot$. The resulting $c(M)$ at low masses is within the uncertainty band of Fig. 1 of Ref. [50].

One additional source of uncertainty is the amount of subhaloes hosted by main haloes. We consider two scenarios—dubbed LOW and HIGH—as extreme cases bracketing the effect of subhaloes. The LOW scenario follows the procedure introduced in Ref. [51] and encodes the results of Ref. [52]. The HIGH scenario stems from the results of Ref. [53] and is implemented by means of the semi-analytical approach described in Ref. [24]. Note that, when subhaloes are included in the computation of the DM-induced γ -ray emission, the last factor in Eq. (2.4) has to be changed into $\int dV \rho_h^2(\mathbf{x}|M, \chi) [1 + B(M, \chi)] / \bar{\rho}_{\text{DM}}^2$, where $B(M, \chi)$ is the so-called subhalo boost. For LOW and HIGH we take $M_{\text{min}} = 10^{-6} M_\odot$.

The blue curves of Fig. 1 show the window function (left panel) of Eq. (2.3) and the average γ -ray intensity (right panel). We choose a benchmark particle physics model with $m_{\text{DM}} = 100$ GeV, $\langle \sigma_a v \rangle = 3 \times 10^{-26} \text{ cm}^3 \text{ s}^{-1}$ and an annihilation channel into $b\bar{b}$. Note that the three clustering scenarios proposed (NS, LOW and HIGH for dotted, solid and dashed curves, respectively) share approximately the same redshift dependence, but they correspond to different intensities for the clumping factor and consequently for the DM-induced γ -ray flux. Note that a comparison with previous works in the literature can be non-trivial, as different groups employ different prescriptions for the DM clustering and, in particular, for the boost factor (see e.g. Refs [23, 24]). Fig. 1 can be useful also as a normalisation test when confronting the result presented in the rest of the paper with other works.

2.1.2 Decaying dark matter

If DM produces γ rays by particle decay ($X = \gamma_{\text{dDM}}$), the source field traces the DM density linearly, i.e. $g_{\gamma_{\text{dDM}}}(\chi, \hat{\mathbf{n}}) = \rho_{\text{DM}}(\chi, \hat{\mathbf{n}})$. Thence, the window function is

$$W^{\gamma_{\text{dDM}}}(\chi) = \frac{\Omega_{\text{DM}} \rho_c}{4\pi} \frac{\Gamma_d}{m_{\text{DM}}} \int_{\Delta E_\gamma} dE_\gamma \frac{dN_d}{dE_\gamma} [E_\gamma(\chi)] e^{-\tau[\chi, E_\gamma(\chi)]}. \quad (2.5)$$

The photon yield, dN_d/dE_γ , is assumed to be the same as for annihilating DM, but with the energy of the process given by $\sqrt{s} = m_{\text{DM}}$ instead of $2m_{\text{DM}}$. In other words, $dN_d/dE_\gamma(E_\gamma) = dN_a/dE_\gamma(2E_\gamma)$ and the kinematic end-point is at $m_{\text{DM}}/2$. The window function and the average emission in the case of decaying DM are shown as green curves in Fig. 1. We choose a benchmark particle physics model with $m_{\text{DM}} = 200$ GeV, $\Gamma_d = 0.33 \times 10^{-27} \text{ s}^{-1}$ and decays into b quarks. Note the redshift scaling similar to the annihilating DM case.

2.2 Astrophysical sources

For astrophysical sources, we choose the source luminosity \mathcal{L} as the characterising parameter for the different sources. For the angular scales of interest in this analysis ($\ell < 1000$), the emission from AGNs and galaxies can be safely considered as point-like. For a power-law

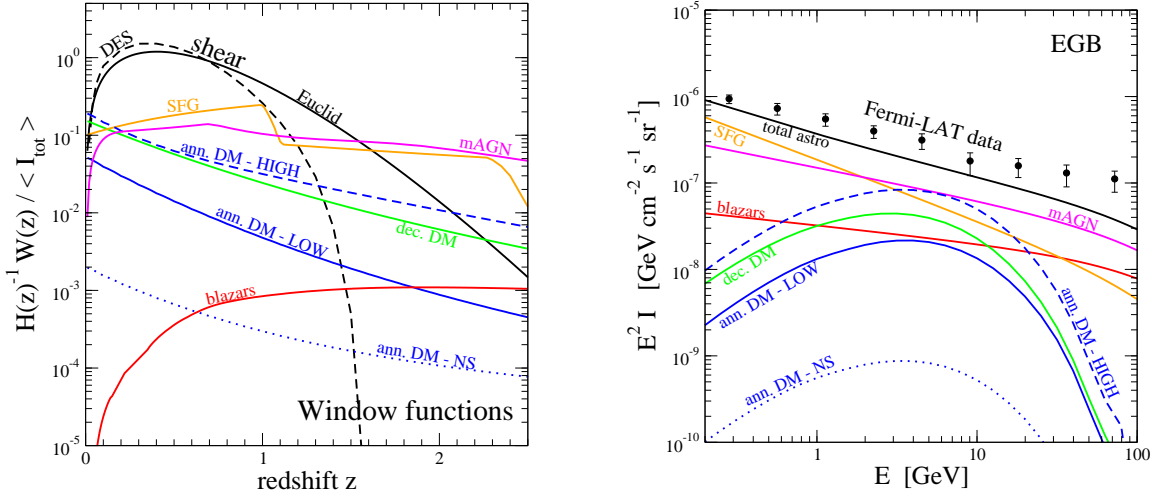


Figure 1. Left: Redshift dependence of the window function for the various signals described in the text. The window functions for γ rays are integrated above $E > 1$ GeV and normalised to the total EGB intensity measured by the Fermi-LAT telescope [54] above 1 GeV, in order to ease comparison. The shear signal is normalised so that the integral of the window function over z is equal to 1. The solid (dashed) blue line corresponds to annihilating DM in the LOW (HIGH) scenario, whilst the dotted blue line represents the NS model. The solid green line stands for decaying DM. The WIMP mass is set to 100 GeV (200 GeV) for annihilating (decaying) DM. The annihilation cross section is $\langle \sigma_a v \rangle = 3 \times 10^{-26} \text{ cm}^3 \text{s}^{-1}$ and the decay lifetime $\Gamma_d = 0.33 \times 10^{-27} \text{ s}^{-1}$. An annihilation/decay channel into b quarks is assumed. Solid red, yellow and magenta curves represent the contributions from blazars, SFGs and mAGNs. The solid (dashed) black lines indicates the window function for the expected cosmic shear from *Euclid* (DES). See the text for the description of the astrophysical sources and of the shear signal. Right: Contributions to the EGB intensity from annihilating DM, decaying DM, blazars, mAGNs, and SFGs. Same models and colour-coding of left panel. The black line shows the sum of the three astrophysical components, whilst Fermi-LAT measurement from Ref. [54] is shown with black data points.

energy spectrum with spectral index α , the window function takes the form Ref. [see e.g. 28]

$$W^{\gamma_i}(\chi) = \frac{A_i(\chi) \langle g_{\gamma_i}(\chi) \rangle}{4\pi E_0^2} \int_{\Delta E_\gamma} dE_\gamma \left(\frac{E_\gamma}{E_0} \right)^{-\alpha_i} e^{-\tau[\chi, E_\gamma(\chi)]}, \quad (2.6)$$

where i stands for blazars, mAGNs or SFGs. The normalisation factor A_i depends on the exact definition of luminosity and $\langle g_{\gamma_i}(\chi) \rangle$ indicates the mean luminosity produced by an unresolved class of objects located at a distance χ . It can be written as

$$\langle g_{\gamma_i}(\chi) \rangle = \int_{\mathcal{L}_{\min}}^{\mathcal{L}_{\max}(F_{\text{sens}}, z)} d\mathcal{L} \mathcal{L} \rho_{\gamma_i}(\mathcal{L}, z), \quad (2.7)$$

where ρ_{γ_i} is the γ -ray luminosity function for source class i . The upper bound, $\mathcal{L}_{\max}(F_{\text{sens}}, z)$, is the luminosity above which an object can be resolved, assuming a sensitivity $F_{\text{sens}} = 2 \times 10^{-9} \text{ cm}^{-2} \text{s}^{-1}$ above 100 MeV typical of Fermi-LAT after 5 years of data taking.² Conversely, the minimum luminosity \mathcal{L}_{\min} depends on the properties of the source class under investigation. The three populations of astrophysical γ -ray emitters (i.e. blazars, mAGNs

²When we consider a larger period of data taking or an improved telescope, we assume that the sensitivity scales as the inverse of squared exposure of the instrument (see Table 3).

and SFGs) are discussed in the following. For each of them we describe the choice of α_i and of the γ -ray luminosity function.

2.2.1 Blazars

Following Ref. [5], we consider flat-spectrum radio quasars and BL Lacertae cumulatively as one unique class of blazars ($X = \gamma_{\text{BLA}}$)³. The common spectral index α_{BLA} is fixed to 2.2 and the γ -ray luminosity \mathcal{L} is computed at 100 MeV, which implies $A_{\text{BLA}}(\chi) = [1 + z(\chi)]^{-\alpha_{\text{BLA}}}$. The lower limit of the integral in Eq. (2.7) is set to $\mathcal{L}_{\text{min}} = 10^{42} \text{ ergs}^{-1}$, corresponding to the lowest luminosity detected (locally) by Fermi-LAT. This assumes that no fainter blazar exists at any redshift.

The γ -ray luminosity function of blazars is computed following the model described in Ref. [4], taking advantage of the well-established correlation between γ -ray and X-ray luminosities. The X-ray luminosity function is taken from Ref. [55]. The numerical value of the parameters characterising the γ -ray luminosity function are fixed to the values provided in Ref. [8], for which unresolved blazars account for about 6% of the Fermi-LAT 1-yr EGB intensity above 1 GeV [54], but to 100% of the EGB auto-correlation APS [25].

The window function and the average emission of unresolved blazars is shown by the solid red lines in Fig. 1. We note that the window function is intrinsically low and it decreases rapidly below $z = 1$. This is due to the fact that we focus only on unresolved sources and Fermi-LAT has already detected a large number of the brightest and/or closest emitters.

2.2.2 Misaligned AGNs

In the case of mAGN ($X = \gamma_{\text{mAGN}}$), we follow Ref. [9], which determines a correlation between the γ -ray luminosity and the core radio luminosity $L_{r,\text{core}}$ at 5 GHz. By means of this correlation it is possible to infer the mAGN γ -ray luminosity function from the study of the radio-loud mAGNs at radio frequencies [56]; we consider the best-fit $\mathcal{L} - L_{r,\text{core}}$ relation from Ref. [9]. We assume an average spectral index α_{mAGN} of 2.37 and \mathcal{L} is defined between 0.1 and 100 GeV, which sets $A_{\text{mAGN}} = (\alpha_{\text{mAGN}} - 2)/[1 + z(\chi)]^2$. The solid magenta lines in Fig. 1 indicate the window function and the average emission for unresolved mAGNs.

2.2.3 Star-forming galaxies

For SFGs ($X = \gamma_{\text{SFG}}$) we take a spectral index $\alpha_{\text{SFG}} = 2.7$, and the γ -ray luminosity \mathcal{L} is computed between 0.1 and 100 GeV. As done in Ref. [12], we assume that the γ -ray and infrared (IR) luminosities are correlated. We adopt the best-fit $\mathcal{L} - L_{\text{IR}}$ relation from Ref. [12] and the IR luminosity function from Ref. [57] (see Ref. [12] for more details). The window function and average emission from unresolved SFGs are the solid yellow lines in Fig. 1. The discontinuity in the window function around $z = 1$ is inherited from the analytic fit to the IR data obtained in Ref. [57] (see however the recent Ref. [14]). Also note that our predictions for the γ -ray flux associated to unresolved SFGs is compatible with the results presented in Ref. [12].

The γ -ray emission produced by the three extragalactic astrophysical populations described above accounts for $\sim 70\%$ of the EGB above 1 GeV (see Fig. 1b). This leaves room for the emission associated to DM, which is the focus of this work (for galactic DM contribution,

³Considering one single population of blazars is well motivated when the shape of the energy spectrum is allowed to depend on the luminosity of the source. In that case, the flexibility of model well reproduces the differences between the two subclasses of blazars [5, 7, 10]. Our approach assumes one common spectral index α_{BLA} and, therefore, is a more simplified description.

see e.g. Ref. [58]). Apart from the extragalactic DM-induced emission described in Secs 2.1.1 and 2.1.2, there may be a contribution associated with annihilations/decays in the DM halo of the Milky Way. This is not included in Fig. 1b and, since it does not correlate with the weak gravitational lensing signal, we do not consider such a component in the present work. Other astrophysical components that can contribute significantly to the EGB intensity are galaxy clusters [59, 60], milli-second pulsars [61, 62] and cascades induced by the interactions of ultra-high-energy cosmic rays with the CMB [63, 64]. However, we expect the inclusion of such additional terms to change the results presented in this paper only marginally.

2.3 Cosmic shear

The presence of intervening matter along the path of photons emitted by distant sources causes gravitational lensing distortions in the images of high-redshift sources. In the weak lensing régime, lensing effects can be evaluated on the unperturbed null-geodesic of the unlensed photon [30]. Such distortions, directly related to the distribution of matter on large scales and to the geometry and dynamics of the Universe, can be decomposed into so-called convergence κ and shear γ [30, 65]. Convergence is a direct estimator of the Newtonian potential fluctuations integrated along the line of sight. On scales $\ell \gtrsim 10$, its APS coincides with that of cosmic shear, it can thus similarly be estimated via the statistical analysis of correlations in the observed source ellipticities (see also Sec. 3.2). Thanks to Poisson's equation, which relates the gravitational potential to the distribution of matter, the weak lensing ($X = \kappa$) window function (for both shear and convergence) is

$$W^\kappa(\chi) = \frac{3}{2} H_0^2 \Omega_m [1 + z(\chi)] \chi \int_\chi^\infty d\chi' \frac{\chi' - \chi}{\chi'} \frac{dN_g}{d\chi'}(\chi'), \quad (2.8)$$

where $dN_g/d\chi$ is the redshift distribution of background galaxies.

The window function of Eq. (2.8) is shown as black lines in Fig. 1a for the expected distribution of background galaxies of DES (dashed curve) and *Euclid* (solid curve). (The surveys will be comprehensively described in Sec. 4.1.)

3 Auto- and cross-correlation angular power spectra

In this section, we describe the formalism used to compute the auto-correlation APS of anisotropies in the γ -ray emission and their cross-correlation with cosmic shear. The APS quantifies the fluctuation amplitude in 2-dimensional sky maps. We define the fluctuation along the line-of-sight direction $\hat{\mathbf{n}}$ as $\delta\mathcal{I}^X(\hat{\mathbf{n}}) = \mathcal{I}^X(\hat{\mathbf{n}}) - \langle\mathcal{I}^X\rangle$ and we expand it in spherical harmonics as

$$\frac{\delta\mathcal{I}^X(\hat{\mathbf{n}})}{\langle\mathcal{I}^X\rangle} = \sum_{\ell,m} a_{\ell,m} Y_{\ell,m}(\hat{\mathbf{n}}). \quad (3.1)$$

The dimensionless $a_{\ell,m}$ coefficients can be written as

$$a_{\ell,m} = \frac{1}{\langle\mathcal{I}^X\rangle} \int d\hat{\mathbf{n}} \delta\mathcal{I}^X(\hat{\mathbf{n}}) Y_{\ell,m}(\hat{\mathbf{n}}) = \int d\hat{\mathbf{n}} \int d\chi f_X(\chi, \hat{\mathbf{n}}) W^X(\chi) Y_{\ell,m}(\hat{\mathbf{n}}), \quad (3.2)$$

where $f_X(\chi, \hat{\mathbf{n}})$ is the fluctuation field, defined as $f_X(\chi, \hat{\mathbf{n}}) = g_X(\chi, \hat{\mathbf{n}})/\langle g_X\rangle - 1$.

From the definition of the APS, $C_\ell^{XY} = (2\ell + 1)^{-1} \sum_{m=-\ell}^\ell \langle a_{\ell,m}^X a_{\ell,m}^{Y*} \rangle$, we eventually obtain (see e.g. Ref. [28])

$$C_\ell^{XY} = \frac{1}{\langle\mathcal{I}^X\rangle\langle\mathcal{I}^Y\rangle} \int d\chi \frac{W^X(\chi)W^Y(\chi)}{\chi^2} P^{XY}\left(k = \frac{\ell}{\chi}, \chi\right). \quad (3.3)$$

Here, $P^{XY}(k, \chi)$ is the 3-dimensional power spectrum (3D PS) of fluctuations in observables X and Y ($X = Y$ for auto-correlation). It is the Fourier transform of the 2-point correlation function of the fluctuation fields, $\langle \tilde{f}_X(\chi, \mathbf{k}) \tilde{f}_Y(\chi, \mathbf{k}') \rangle = (2\pi)^3 \delta^3(\mathbf{k} - \mathbf{k}') P^{XY}(k, \chi)$. For the computation of P^{XY} , we adopt the so-called halo-model approach. Following Ref. [66], we assume that each fluctuation field is a sum of discrete seeds identified by their position and one characteristic quantity—the halo mass M in the case of weak lensing or of the γ -ray emission produced by DM, and the source luminosity \mathcal{L} in the case of the γ -ray signal from astrophysical sources. The details of the computation of the 3D PS have been recently reviewed in Ref. [28]. The 3D PS can be written as the sum of two contributions, namely a 1-halo P_{1h} and a 2-halo P_{2h} term. The former accounts for the correlation inside the same object, whilst the latter describes the correlations between two distinct haloes.

The window functions entering Eq. (3.3) have already been introduced in Sec. 2 for each class of sources. In the next sections, we discuss the various ingredients required for the computation of P_{1h} and P_{2h} . Eq. (3.3) is obtained under Limber's approximation [67, 68], which links the physical wavenumber k to the angular multipole ℓ . Such an approximation is known to hold for $\ell \gg 1$; this condition is satisfied in this paper, since we normally consider scales $\ell \gtrsim 100$.

3.1 Angular power spectrum of γ -ray emission

Since we consider four γ -ray emitters (three astrophysical populations plus DM haloes), the auto-correlation APS of the total γ -ray emission is given by the sum of the auto-correlation APS of each class of emitters plus their relative cross-correlations. The APS of the total γ -ray emission reads (we do not specify if DM is annihilating or decaying)

$$C_\ell^\gamma = C_\ell^{\gamma\text{DM}} + C_\ell^{\gamma\text{BLA}} + C_\ell^{\gamma\text{mAGN}} + C_\ell^{\gamma\text{SFG}} + 2C_\ell^{\gamma\text{DM}\gamma\text{BLA}} + 2C_\ell^{\gamma\text{DM}\gamma\text{mAGN}} + 2C_\ell^{\gamma\text{DM}\gamma\text{SFG}} + 2C_\ell^{\gamma\text{BLA}\gamma\text{mAGN}} + 2C_\ell^{\gamma\text{BLA}\gamma\text{SFG}} + 2C_\ell^{\gamma\text{mAGN}\gamma\text{SFG}}. \quad (3.4)$$

3.1.1 Dark matter

Let us start with the case of decaying DM, where the density field is given by the DM density distribution, namely $g_{\gamma\text{dDM}}(\mathbf{x}) = \rho_{\text{DM}}(\mathbf{x})$. This means $f_{\gamma\text{dDM}}(\mathbf{x}) = \delta(\mathbf{x})$, where $\delta(\mathbf{x})$ is the DM density contrast. Therefore, the 3D PS quantifies the correlation between two density fluctuations δ , and its 1- and 2-halo terms are

$$P_{1h}^{\delta\delta}(k, z) = \int_{M_{\min}}^{M_{\max}} dM \frac{dn}{dM} \tilde{v}^2(k|M), \quad (3.5)$$

$$P_{2h}^{\delta\delta}(k, z) = \left[\int_{M_{\min}}^{M_{\max}} dM \frac{dn}{dM} b_h(M) \tilde{v}(k|M) \right]^2 P_{\text{lin}}(k, z), \quad (3.6)$$

where $\tilde{v}(k|M)$ is the Fourier transform of $\rho_{\text{DM}}(\mathbf{x}|M)/\bar{\rho}_{\text{DM}}$, P_{lin} is the linear matter power spectrum and b_h is the bias between the haloes and matter distribution, described according to Ref. [69].

Conversely, in the case of annihilating DM, the source field scales with the square of the DM density, viz. $g_{\gamma\text{aDM}}(\mathbf{x}) = \rho_{\text{DM}}^2(\mathbf{x})$. Then, the 3D PS correlates fluctuations in the squared

density field δ^2 , i.e.

$$P_{1h}^{\delta^2\delta^2}(k, z) = \int_{M_{\min}}^{M_{\max}} dM \frac{dn}{dM} \left[\frac{\tilde{u}(k|M)}{\Delta^2} \right]^2, \quad (3.7)$$

$$P_{2h}^{\delta^2\delta^2}(k, z) = \left[\int_{M_{\min}}^{M_{\max}} dM \frac{dn}{dM} b_h(M) \frac{\tilde{u}(k|M)}{\Delta^2} \right]^2 P_{\text{lin}}(k, z), \quad (3.8)$$

where $\tilde{u}(k|M)$ is the Fourier transform of $\rho_{\text{DM}}^2(\mathbf{x}|M)/\bar{\rho}_{\text{DM}}^2$.

The linear matter power spectrum is well constrained by cosmological observations and N -body simulations for masses above $10^{10} M_{\odot}$. In the case of a decaying DM candidate, the bulk of the signal comes from large haloes. Therefore, the predicted APS is rather robust and the auto-correlation APS (for decaying DM) is plotted as the solid green line in Fig. 2a. In the case of annihilating DM, the APS is affected by uncertainties related to the clustering at small masses mentioned in Sec. 2.1.1, i.e. the amount of subhaloes and the value of M_{\min} (see e.g. Ref. [24] for further discussions). These uncertainties affect both the normalisation and angular shape of the APS. The former is proportional to the intensity of the emission, so we expect a similar behaviour to what depicted in Fig. 1.

In Fig. 2 (left panel), the auto-correlation APS for annihilating DM is plotted for the NS (dotted, blue line), LOW (solid, blue line) and HIGH (dashed, blue line) scenarios. To compare more easily between different shapes for the APS, we use a common, arbitrary normalisation. As the contribution to the total signal from large masses increases, the relative size of the 1-halo term of the 3D PS increases with respect to the 2-halo term (on large scales), leading to a steepening of the APS at ℓ below few hundreds. Such behaviour is straightforward to visualise by comparing the HIGH, LOW and NS scenarios. Indeed, the higher subhalo contribution in the HIGH case leads to a higher boost in large haloes with respect to the other scenarios, and thus to an APS growing more rapidly for $\ell \lesssim 100$. In general, in the presence of DM subhaloes, DM haloes with medium to large masses dominate the signal. This implies that, in these cases, the 3D PS drops at small scales. In the NS scenario, on the other hand, (relatively) low masses give a significant contribution and the associated 1-halo term extends to smaller scales. Consequently, the APS raises at large multipoles. This can be seen in the left panel of Fig. 2 in the large ℓ régime, where the 1-halo term dominates over the 2-halo term. The APS of the NS scenario—where there are no subhaloes—is larger than the LOW and HIGH cases for $\ell > 300$. This trend is compatible with what found in Ref. [23].

We emphasise that, contrarily to some other works in the literature, we choose to normalise the 3D PS by $\langle g_X \rangle$ (i.e. proportional to Δ^2 , in the annihilating DM case), which is re-absorbed in the window function. By doing so, the P_{2h} is normalised to (approximately) the linear matter power spectrum for all components—except for the multiplicative bias term.

3.1.2 Astrophysical sources

For γ rays induced by astrophysical sources, we work under the hypothesis that their distribution traces the underlying matter field. Then, equations similar to Eqs (3.5) to (3.8) can still be used to quantify the 3D 1-halo and 2-halo PS, with some caveats. First, the quantity that characterises the sources is not longer their mass, but rather their luminosity \mathcal{L} . Secondly, instead of the halo mass function dn/dM , the γ -ray luminosity function must be considered. Finally, instead of the halo bias b_h , each class of sources is characterised by its own bias factor $b_{\gamma_i}(\mathcal{L}, z)$. Furthermore, note that, being point-like, the 1-halo term for astrophysical sources loses any dependence on k , thus becoming Poisson-like. Hence, the

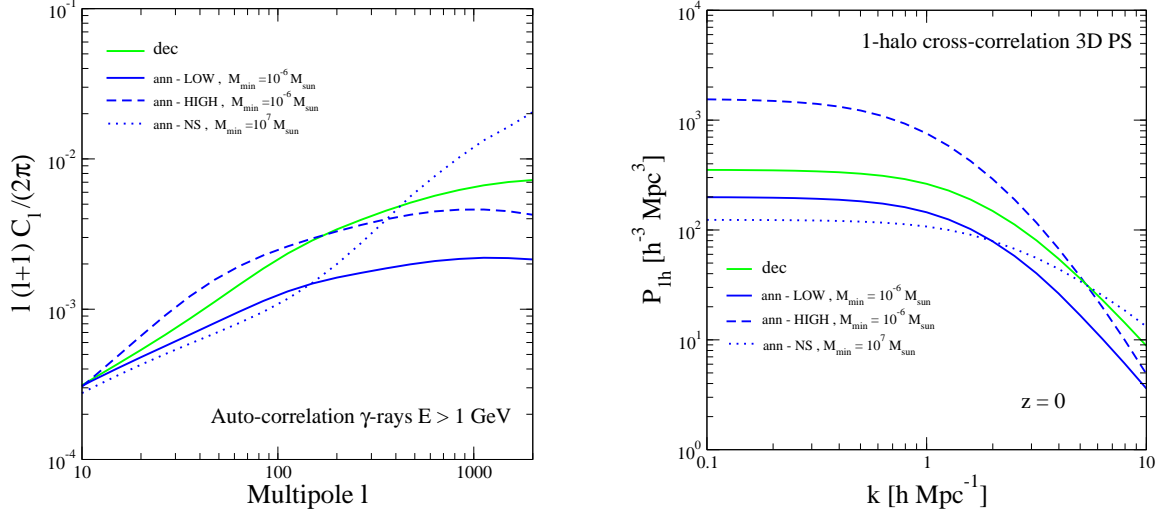


Figure 2. Left: Auto-correlation APS of the γ -ray emission for annihilating (blue) and decaying (green) DM. Arbitrary normalisation. The DM microscopic properties are chosen as in Fig. 1. The solid (dashed) blue line refers to the LOW (HIGH) scenario, whilst the dotted one is for NS. Right: 1-halo term of the 3D PS for the cross-correlation of cosmic shear with DM-induced γ -ray emission at $z = 0$. The same scenarios and line styles are used as in the left panel.

3D PS can be written as

$$P_{1h}^{\delta\delta}(k, z) = \int_{\mathcal{L}_{\min}(z)}^{\mathcal{L}_{\max}(z)} d\mathcal{L} \rho_{\gamma_i}(\mathcal{L}, z) \left(\frac{\mathcal{L}}{\langle g_{\gamma_i} \rangle} \right)^2, \quad (3.9)$$

$$P_{2h}^{\delta\delta}(k, z) = \left[\int_{\mathcal{L}_{\min}(z)}^{\mathcal{L}_{\max}(z)} d\mathcal{L} \rho_{\gamma_i}(\mathcal{L}, z) b_{\gamma_i}(\mathcal{L}, z) \frac{\mathcal{L}}{\langle g_{\gamma_i} \rangle} \right]^2 P_{\text{lin}}(k, z). \quad (3.10)$$

If the γ -ray emission of a population of sources is dominated by a few very bright objects (but still below the detection threshold of the telescope), the 1-halo term will be larger than the 2-halo and the auto-correlation APS will therefore be Poissonian, with no dependence on the source clustering. On the other hand, the auto-correlation APS can have some sensitivity to the distribution of the sources if they are faint but numerous. Indeed, in this case the 2-halo term will dominate over the Poissonian 1-halo term. Following our description of astrophysical sources in Sec. 2.2, the auto-correlation APS of blazars and mAGNs is Poissonian over the whole multipole range considered here ($\ell < 1000$), whilst for SFGs, some dependence on the 2-halo term is present below $\ell = 500$.

The cross-correlation terms in Eq. (3.4) includes correlations between two different astrophysical populations or between an astrophysical population and DM. They provide subdominant contributions to the total APS, but, for completeness, we list here the expression of their 3D PS.

The 3D PS for the correlations between one astrophysical class of γ -ray emitter and

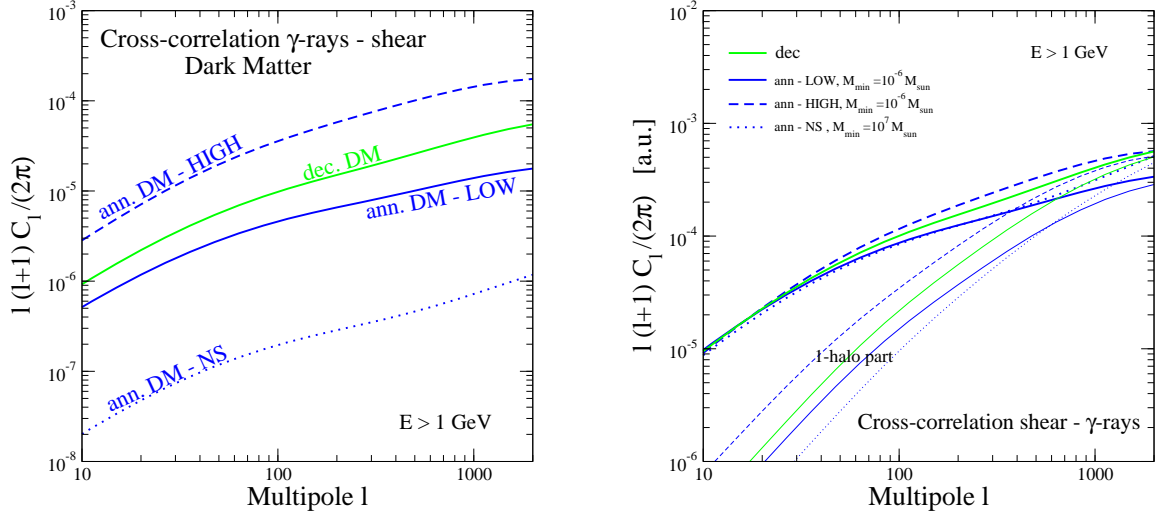


Figure 3. Cross-correlation APS of the DM-induced γ -ray emission for $E > 1$ GeV and the weak lensing signal. The DM microscopic properties are chosen as in Fig. 1. The solid (dashed) blue line refers to the LOW (HIGH) scenario, whilst the dotted one is for NS. In the right panel, we show the 1-halo terms of the total APS with thin lines, and curves are arbitrarily normalised to better compare their angular shapes.

decaying DM reads

$$P_{1h}^{\delta\delta}(k, z) = \int_{\mathcal{L}_{\min}(z)}^{\mathcal{L}_{\max}(z)} d\mathcal{L} \rho_{\gamma_i}(\mathcal{L}, z) \frac{\mathcal{L}}{\langle g_{\gamma_i} \rangle} \tilde{v}[k|M(\mathcal{L})] \quad (3.11)$$

$$P_{2h}^{\delta\delta}(k, z) = \left[\int_{\mathcal{L}_{\min}(z)}^{\mathcal{L}_{\max}(z)} d\mathcal{L} \rho_{\gamma_i}(\mathcal{L}, z) b_{\gamma_i}(\mathcal{L}, z) \frac{\mathcal{L}}{\langle g_{\gamma_i} \rangle} \right] \left[\int_{M_{\min}}^{M_{\max}} dM \frac{dn}{dM} b_h(M) \tilde{v}(k|M) \right] P_{\text{lin}}(k, z). \quad (3.12)$$

Otherwise, in the case of annihilating DM, one has

$$P_{1h}^{\delta\delta^2}(k, z) = \int_{\mathcal{L}_{\min}(z)}^{\mathcal{L}_{\max}(z)} d\mathcal{L} \rho_{\gamma_i}(\mathcal{L}, z) \frac{\mathcal{L}}{\langle g_{\gamma_i} \rangle} \frac{\tilde{u}[k|M(\mathcal{L})]}{\Delta^2} \quad (3.13)$$

$$P_{2h}^{\delta\delta^2}(k, z) = \left[\int_{\mathcal{L}_{\min}(z)}^{\mathcal{L}_{\max}(z)} d\mathcal{L} \rho_{\gamma_i}(\mathcal{L}, z) b_{\gamma_i}(\mathcal{L}, z) \frac{\mathcal{L}}{\langle g_{\gamma_i} \rangle} \right] \left[\int_{M_{\min}}^{M_{\max}} dM \frac{dn}{dM} b_h(M) \frac{\tilde{u}(k|M)}{\Delta^2} \right] P_{\text{lin}}(k, z).$$

Lastly, the 2-halo term of the cross-correlation 3D PS for two γ -ray astrophysical populations is

$$P_{2h}^{\delta\delta}(k, z) = \left[\int_{\mathcal{L}_{\min}(z)}^{\mathcal{L}_{\max}(z)} d\mathcal{L} \rho_{\gamma_i}(\mathcal{L}, z) b_{\gamma_i}(\mathcal{L}, z) \frac{\mathcal{L}}{\langle g_{\gamma_i} \rangle} \right] \left[\int_{\tilde{\mathcal{L}}_{\min}(z)}^{\mathcal{L}_{\max}(z)} d\tilde{\mathcal{L}} \rho_{\gamma_j}(\tilde{\mathcal{L}}, z) b_{\gamma_j}(\tilde{\mathcal{L}}, z) \frac{\tilde{\mathcal{L}}}{\langle g_{\gamma_j} \rangle} \right] P_{\text{lin}}(k, z). \quad (3.14)$$

Here, the term $P_{1h}^{\delta\delta} = 0$ since we approximate astrophysical sources as point-like and two distinct objects cannot be in the same point.

Note that in Eqs (3.11) and (3.13), a relation between the source luminosity \mathcal{L} and the mass M of host is required. Such a relation is not well established and different prescriptions

can lead to very different results for the 1-halo terms. We will discuss it in more details in the following section.

To summarise, in order to estimate the contribution of astrophysical sources to the APS, four ingredient are needed: *i*) the γ -ray luminosity function of the specific source class; *ii*) the various energy spectra; *iii*) the relation between the γ -ray luminosity and the mass of the host DM halo, $M(\mathcal{L})$; and *iv*) the bias b_{γ_i} . The last quantity can be computed in terms of the halo bias $b_{\gamma_i}(\mathcal{L}, z) = b_h[M(\mathcal{L}), z]$, for which the $M(\mathcal{L})$ relation is once more required. We note that, since at low z the halo bias b_h is $\mathcal{O}(1)$, the 2-halo term is often only very mildly dependent on $M(\mathcal{L})$.

3.2 Cross-correlation of cosmic shear and γ -ray emission

In a perturbed Universe around a (flat) Friedmann-Lemaître-Robertson-Walker background, the line element reads

$$ds^2 = -(1 + 2\Phi) dt^2 + a^2(t) [(1 + 2\Psi) (d\chi^2 + \chi^2 d\Omega^2)], \quad (3.15)$$

where Φ and Ψ are the two Bardeen's metric potentials and Ω is the solid angle. In such a perturbed Universe, a light ray coming towards us from a distant source is deflected by an angle proportional to the transverse gradient of $\Phi - \Psi$ (see e.g. Refs [30, 32]). Therefore, the source of weak lensing distortions is the so-called deflecting potential $\Upsilon = (\Phi - \Psi)/2$. However, in general relativity (and in the absence of anisotropic stress) we have that $\Phi = -\Psi$ and the deflecting potential is thus simply (twice) the Newtonian potential Φ itself. By means of Poisson's equation, fluctuations in the potential correspond to fluctuations in the matter distribution, which plays directly the rôle of the fluctuation field $f_\kappa(\hat{\mathbf{n}}, \chi)$ in Eq. (3.2).

The cross-correlation APS between the cosmic shear and the γ -ray emitter X follows from Eq. (3.3) (see also Paper I and Ref. [28]) and takes the form

$$C_\ell^{X\kappa} = \frac{1}{\langle \mathcal{I}^X \rangle \langle \mathcal{I}^\kappa \rangle} \int d\chi \frac{W^X(\chi) W^\kappa(\chi)}{\chi^2} P^{X\kappa} \left(k = \frac{\ell}{\chi}, \chi \right). \quad (3.16)$$

The total cross-correlation APS is the sum of contributions of the four classes of sources considered, i.e.

$$C_\ell^{\gamma\kappa} = C_\ell^{\gamma\text{DM}\kappa} + C_\ell^{\gamma\text{BLA}\kappa} + C_\ell^{\gamma\text{mAGN}\kappa} + C_\ell^{\gamma\text{SFG}\kappa}. \quad (3.17)$$

3.2.1 Dark matter

In the case of decaying DM, both the DM-induced γ -ray emission and cosmic shear linearly depend upon the DM density. Therefore, the 3D cross-correlation PS is equivalent to that of the auto-correlation for decaying DM and is given by Eqs (3.5) and (3.6). The 1-halo term of the 3D PS $P_{1h}^{\delta\delta}$ is the solid, green line in Fig. 2 (left panel).

For the case of annihilating DM, the 1-halo and 2-halo terms of the 3D cross-correlation PS are

$$P_{1h}^{\delta\delta^2}(k, z) = \int_{M_{\min}}^{M_{\max}} dM \frac{dn}{dM} \tilde{v}(k|M) \frac{\tilde{u}(k|M)}{\Delta^2}, \quad (3.18)$$

$$P_{2h}^{\delta\delta^2}(k, z) = \left[\int_{M_{\min}}^{M_{\max}} dM \frac{dn}{dM} b_h(M) \tilde{v}(k|M) \right] \left[\int_{M_{\min}}^{M_{\max}} dM \frac{dn}{dM} b_h(M) \frac{\tilde{u}(k|M)}{\Delta^2} \right] P_{\text{lin}}(k, z). \quad (3.19)$$

The 2-halo term $P_{2h}^{\delta\delta^2}$ is fairly insensitive to the uncertainties associated to the clustering of haloes at small masses. Their effect mainly alter the bias factor, but no appreciable changes in the shape of the power spectrum are induced. On the other hand, those uncertainties have a heavier impact on the 1-halo term. The right panel of Fig. 2 shows the 1-halo term in the 3D PS $P_{1h}^{\delta\delta^2}$. The blue solid (dashed) curve refers to the LOW (HIGH) scenario, whilst the blue dotted line stands for the NS case. As discussed above, large subhalo boosts increase the contribution of the most massive haloes and the 1-halo power spectrum is then approximately an order of magnitude larger for the HIGH scenario than for the LOW case, at large scales, i.e. low values of k . The picture is opposite at small scales, where the cases with a larger contribution from less massive haloes (especially the NS model) have a larger 1-halo term.

Fig. 3 shows the cross-correlation APS between cosmic shear and DM. Blue (green) lines stand for annihilating (decaying) DM. The same line styles as in Fig. 2 are used to indicate the three different models for the clustering of DM haloes. Despite the differences amongst the three scenarios discussed in Fig. 2 (left panel), the shape of the cross-correlation APS is now quite robust and it does not depend much on the amount of subhaloes or the value of M_{\min} . This is because those uncertainties mainly affect the 1-halo term (shown separately in the lower set of lines), which starts to dominate only at very large multipoles, $\ell > 500$. In the right panel of Fig. 3, we again adopted arbitrary normalisation to focus on the APS shape. Even if the shape of the APS does not depend dramatically on the clustering model, its normalisation does (as clear from the left panel), since it is proportional to the intensity (see also Fig. 1, right panel).

3.2.2 Blazars

Moving to the discussion of the cross-correlation 3D PS between cosmic shear and astrophysical γ -ray emitters, the computation of the cross-correlation PS relies on the knowledge of how the luminosity of the source, \mathcal{L} , relates to the mass of the DM halo which hosts it.

For the case of blazars, the $M(\mathcal{L})$ relation is modelled from the results of Ref. [70]. A simple power-law scaling $M = A(z)\mathcal{L}_X^{\Gamma(z)}$ between the X-ray luminosity, \mathcal{L}_X , and the mass of the host DM halo, M , is found to reproduce well the abundance of X-ray selected AGNs at different redshifts (see their Fig. 6 and Table 1). Then, the X-ray luminosity is linked to the that of γ rays through the correlation already discussed and employed in Sec. 2.2.1. This will represent our fiducial model for the $M(\mathcal{L})$ relation for blazars. The corresponding $P_{1h}(k, z = 0)$ is plotted in Fig. 4 as a solid line.

Differently, Ref. [71] considers another approach, linking the γ -ray luminosity of a blazar to the mass of the super-massive black hole (SMBH) powering the AGN. In turn, that is related to the DM halo mass, leading to $M = 10^{11.3} M_{\odot} (\mathcal{L}/10^{44.7} \text{ erg s}^{-1})^{1.7}$ (what the authors of Ref. [71] call ‘model A’) or to $M = 10^{13} M_{\odot} (\mathcal{L}/10^{44} \text{ erg s}^{-1})^{1.7}$ (their ‘model B’). Both (dashed and lower dotted lines in Fig. 4) produce a P_{1h} that is smaller than the one obtained with the $M(\mathcal{L})$ relation from Ref. [70]. The prediction for model A (i.e. the smaller of the two) is approximately 4 orders of magnitude below our fiducial model, for $k < 10 \text{ Mpc}/h$. We consider this as our lower limit for the 1-halo 3D PS for blazars. Our upper limit is the same adopted in Paper I, i.e. a modification of model B from Ref. [71], with a larger normalisation, namely $M = 10^{13} M_{\odot} (\mathcal{L}/10^{42} \text{ erg s}^{-1})^{1.7}$ (see the upper dotted line in Fig. 4). This corresponds to a PS approximately 2 orders of magnitude larger than our fiducial model. The uncertainty generated by the $M(\mathcal{L})$ relation is large and it propagates to the 1-halo term of the 3D cross-correlation PS. However, as we shall see later, the blazar

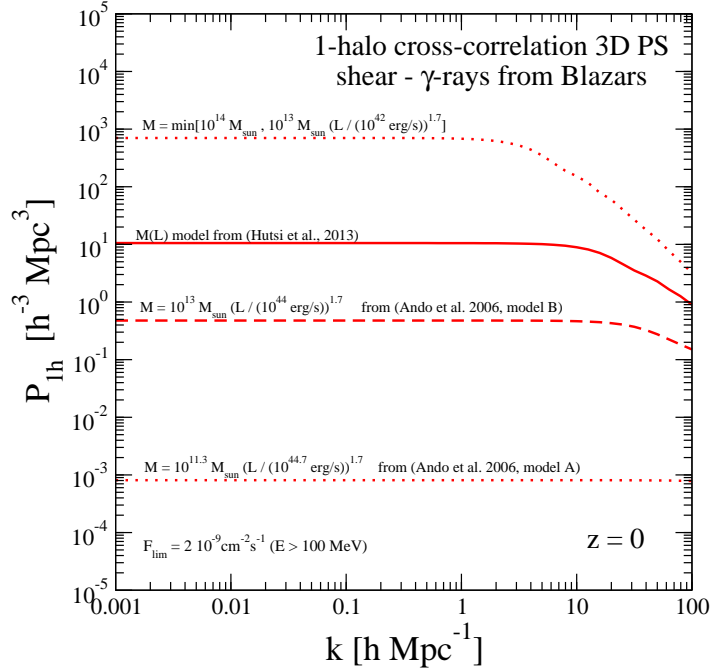


Figure 4. 1-halo term of the 3D cross-correlation PS between cosmic shear and γ rays from unresolved blazars. The different lines correspond to different choices of the $M(\mathcal{L})$ relation. See text for details.

contribution to the total cross-correlation APS is subdominant and such uncertainties will not therefore affect our conclusions.

3.2.3 Misaligned AGNs

The relation $M(\mathcal{L})$ for mAGNs can be inferred through a chain of correlations. We first make use of the relation between the γ -ray luminosity and the core radio luminosity $L_{r,\text{core}}$, as done already in Sec. 2.2.2. Then, $L_{r,\text{core}}$ is related to the mass of the accreting SMBH, M_\bullet , as in Ref. [72]. The $L_{r,\text{core}} - M_\bullet$ relation is affected by considerable scatter, as found e.g. in Ref. [73]. We find that allowing the normalisation of $M_\bullet(L_{r,\text{core}})$ to vary in the range between 0.1 and 2.5 generates an uncertainty band that encompasses well the data, see Fig. 8 of Ref. [73].

Finally, the mass of the SMBH is related to the mass of the host DM halo by following Ref. [70] (which is in turn based on Ref. [74]). However, we found that this procedure, when applied to the sample of mAGNs detected by Fermi-LAT [9], generates SMBH masses that are too large. This is probably because it is based on a galaxy population different from mAGNs. Thus, the $M - M_\bullet$ relation of Ref. [70] has been renormalised, in order to reproduce the characteristics of M 87, whose SMBH mass has been measured as $6.6 \times 10^9 M_\odot$ [75] and with a DM-halo mass of $2.2 \times 10^{13} M_\odot$ [76]. The 1-halo 3D PS obtained by means of this $M(\mathcal{L})$ relation is plotted in Fig. 5 as a solid, magenta line (see also Appendix A) and will be our fiducial model. The two dashed lines quantify the uncertainty from the scatter in the $L_{r,\text{core}} - M_\bullet$ relation mentioned above.

We also derive the relation between the γ -ray luminosity and the mass of the SMBH empirically, by using the measurements available in the literature on the mass of SMBHs for the mAGNs detected by Fermi-LAT (see Appendix A and Fig. 17). The result can be seen

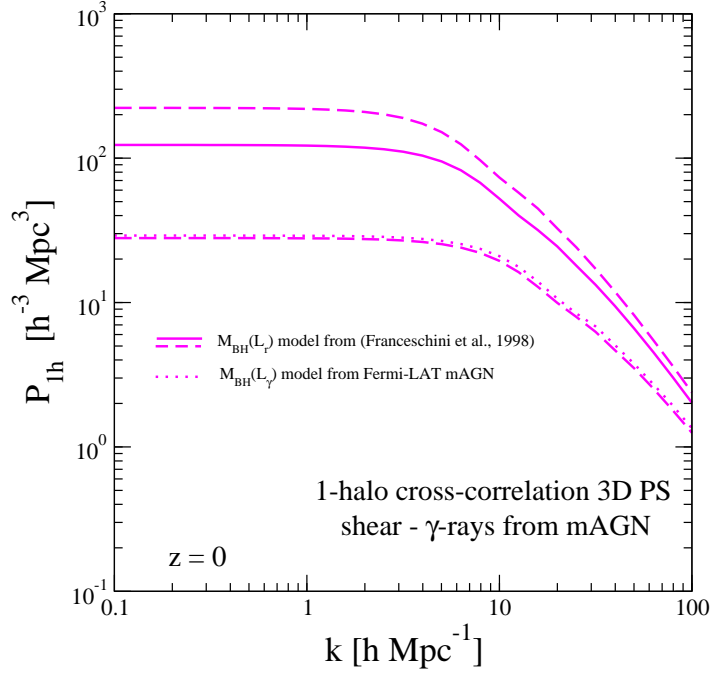


Figure 5. 1-halo term of the 3D cross-correlation PS between cosmic shear and γ rays from unresolved mAGNs. The different lines correspond to different choices of the $M(\mathcal{L})$ relation. See text for details.

from the dotted line in Fig. 5 and is within the uncertainty band of the model described above.

3.2.4 Star-forming galaxies

In Ref. [12], the 8 SFGs detected by Fermi-LAT (together with the upper limit from the non-detection of 64 bright IR galaxies) were employed to determine a relation between the γ -ray luminosity and the star-formation rate (SFR) (see Figs. 3 and 4 of Ref. [12]). A correlation between \mathcal{L} and SFR is expected in many models describing the γ -ray emission of SFGs [13, 77]. Then, the mass of the DM halo can be derived from the SFR through the Kennicutt-Schmidt law, which links the SFR and mass of gas, and then assuming a certain DM-to-gas ratio. The resulting $M(\mathcal{L})$ relation is normalised to the properties of the Milky Way and it is used in Paper I. It shows that M can be well approximated by $\simeq 10^{12} M_{\odot} \sqrt{\mathcal{L}/10^{39} \text{ erg s}^{-1}}$. This will represent our fiducial case and the corresponding 1-halo 3D PS is shown as a solid, yellow line in Fig. 6. The dashed and dotted yellow curves are taken from Paper I to provide reasonable uncertainties to this model.

An alternative relation between SFR and the mass of the host DM halo can be obtained from the empirical model for star formation proposed in Ref. [78] (see their Fig. 9). Together with the \mathcal{L} -SFR relation from Ref. [12], this provide a new $M(\mathcal{L})$, and the corresponding 1-halo 3D PS is plotted in Fig 6 by means of green lines. Model III from Ref. [78] is adopted and the dashed green lines indicate the uncertainty induced when the parameters of the model are left free to vary (within the 95% C.L. region).

As done in the previous section, we can also proceed empirically and derive the $M(\mathcal{L})$ relation by means of a power-law fit considering the SFGs detected by Fermi-LAT for which we have estimates of the mass of their DM halo (see Appendix B and Fig. 18). We obtain

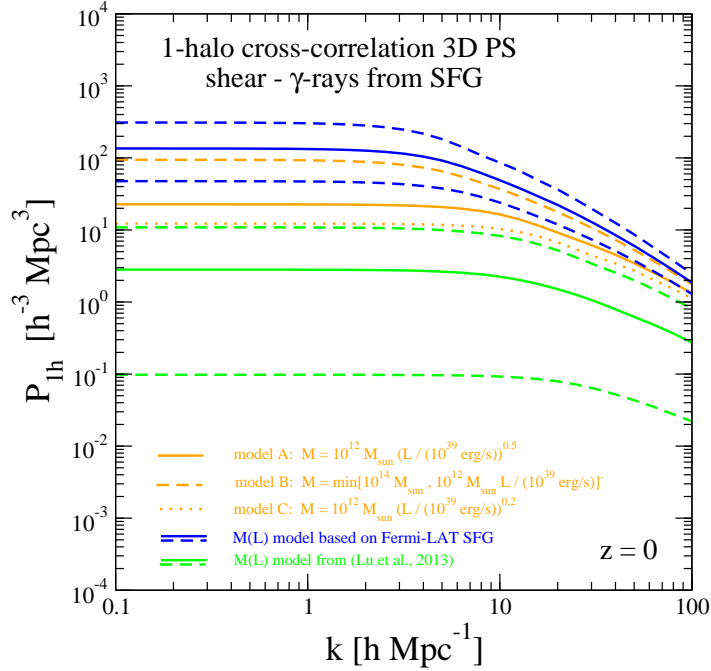


Figure 6. 1-halo term of the 3D cross-correlation PS between cosmic shear and γ rays from unresolved SFGs. The different lines correspond to different choices of the $M(\mathcal{L})$ relation. See text for details.

$M = 10^{11.9 \pm 0.5} M_{\odot} (\mathcal{L} / 10^{38} \text{ erg s}^{-1})^{0.71}$. Such a relation is valid only at $z = 0$ because the SFGs employed in the fit are local. Thus, we assume the same dependence on z as in the models from Ref. [78]. The corresponding 1-halo 3D PS is shown in Fig. 6 as a blue, solid and dashed, curves.

In the left panel of Fig. 7, we show the impact of the assumed $M(\mathcal{L})$ relation on the predicted cross-correlation APS for the astrophysical γ -ray emitters (red for blazars, magenta for mAGNs and yellow for SFGs). The solid lines correspond to the fiducial cases described above, whilst for the upper (lower) dashed lines we considered the largest (smallest) $M(\mathcal{L})$ amongst the alternatives presented in the previous sections (see Figs 4-6). It is important to notice that, for *all* the classes of sources considered here, the lower edge of the uncertainty band corresponds to a case where the 1-halo term is subdominant in the multipole range of interest ($\ell \lesssim 1000$). Even, for the upper edge of the uncertainty band, the cross-correlation APS starts to be sensitive to the 1-halo term only at around $\ell = 500$, i.e. where the sensitivity is already quite low when using Fermi-LAT data. The effect of the $M(\mathcal{L})$ relation on the 2-halo term is only through the bias and it can affect low multipoles ℓ through an $\mathcal{O}(1)$ normalisation (as visible in Fig. 7, left panel). For simplicity this effect will be neglected in the following. As a net result, our prediction for the cross-correlation signal will not be spoiled by the huge uncertainties associated to $M(\mathcal{L})$ and discussed above. To compare the cross-correlation with astrophysical sources and that induced by DM, one should compare the left panels of Figs 7 and 3.

The cross-correlation APS between cosmic shear and astrophysical sources $C_{\ell}^{\gamma i \kappa}$ will be computed assuming the fiducial models for $M(\mathcal{L})$ described above. However, in order to take into account the uncertainty associated to the $M(\mathcal{L})$ relations, we introduce the coefficients \mathcal{A}_{BLA} , $\mathcal{A}_{\text{mAGN}}$ and \mathcal{A}_{SFG} . They will act as normalisation factors multiplying the 1-halo

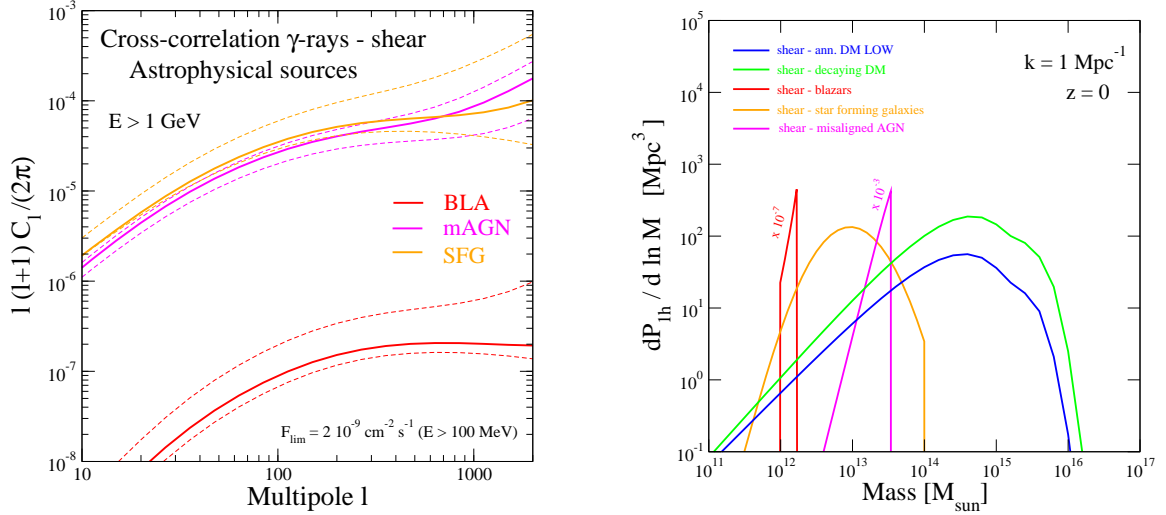


Figure 7. Left: Cross-correlation APS between cosmic shear and γ rays from blazars (red), mAGNs (magenta) and SFGs (yellow). Different curves correspond to different choices of $M(\mathcal{L})$ with solid lines being our fiducial models and dashed lines depicting the upper and lower limits from Figs 4-6 (see text for details). Right: The quantity $dP_{1h}/d \ln M$ as a function of the mass of the DM halo, M . $dP_{1h}/d \ln M$ is the integrand of the 1-halo term P_{1h} of the 3D cross-correlation PS (at $z = 0$ and $k = 1 \text{ Mpc}^{-1}$) and it is plotted here for the different γ -ray emitters considered in this work. The blue line corresponds to annihilating DM (for a LOW scenario), whilst the green one is for decaying DM. The red (magenta) line stands for blazars (mAGNs) and it has been multiplied by 10^{-7} (10^{-3}) to ease the comparison. The yellow one is for SFGs.

term of the APS, shifting it up and down with respect to the fiducial case, corresponding to $\mathcal{A}_i = 1$. The range of variation for these normalisations is determined in order to encompass the uncertainty on $M(\mathcal{L})$ discussed above and it is derived from Figs. 4-6. In particular, \mathcal{A}_{BLA} is allowed to vary between 0.05 and 50, \mathcal{A}_{SFG} between 0.1 and 10 and \mathcal{A}_{mAGN} between 0.2 and 2.

Contrarily to what happens for astrophysical sources, the 1-halo term of the cross-correlation APS with DM-induced γ -ray emission is large. This can be seen by comparing the right panel of Fig. 2b and Figs 4-6. It is related to the fact that, for DM, the cross-correlation with cosmic shear is dominated by haloes with $M \gtrsim 10^{14} M_\odot$, which generate a large gravitational lensing signal. However, these are much larger than the haloes hosting unresolved astrophysical emitters. This is shown in Fig. 7 (right panel), where we plot the quantity $dP_{1h}(M)/d \ln M$, namely, the integrand of the 1-halo term of the 3D PS of the cross-correlation between cosmic shear and γ -ray emission (at $z = 0$ and for $k = 1 \text{ Mpc}^{-1}$). The solid, blue line corresponds to the case of annihilating DM for the LOW scenario, whilst the green line is for decaying DM. Red, magenta and yellow curves stand for blazars, mAGNs and SFGs. Note that, as discussed above, the blue and green lines peak at larger masses and are characterised by a larger area below the curves.

The right panel of Fig. 7 also helps us to understand the scaling in Figs 4-6. Having a $M(\mathcal{L})$ relation that implies a larger (lower) M for a given \mathcal{L} , i.e. a large (small) \mathcal{A}_i , will shift the peak of the curves in Fig. 7b to larger (smaller) masses, increasing (decreasing) the overall P_{1h} .

For the sake of clarity, in Table 1 we summarise the name of all the classes of γ -ray

Acronym	Brief description
<i>d</i> DM	Decaying DM: halo mass function from Ref. [46]; NFW density profile; $M_{\min} = 10^{-6} M_{\odot}$; $c(M)$ relation from Ref. [48] above $10^{10} M_{\odot}$ and from Ref. [49] below; bias from Ref. [69].
<i>a</i> DM NS	Annihilating DM, no-substructure scenario: halo mass function from Ref. [46]; NFW density profile; $M_{\min} = 10^7 M_{\odot}$; $c(M)$ relation from Ref. [48] above $10^{10} M_{\odot}$ and from Ref. [49] below; no subhaloes; bias from Ref. [69].
<i>a</i> DM LOW	Annihilating DM, LOW substructure scenario: halo mass function from Ref. [46]; NFW density profile; $M_{\min} = 10^7 M_{\odot}$; $c(M)$ relation from Ref. [48] above $10^{10} M_{\odot}$ and from Ref. [49] below; subhaloes included as in Ref. [52]; bias from Ref. [69].
<i>a</i> DM HIGH	Annihilating DM, HIGH substructure scenario: halo mass function from Ref. [46]; NFW density profile; $M_{\min} = 10^7 M_{\odot}$; $c(M)$ relation from Ref. [48] above $10^{10} M_{\odot}$ and from Ref. [49] below; subhaloes included as in Ref. [53]; bias from Ref. [69].
BLA	Blazars: power-law energy spectrum with $\alpha_{\text{BLA}} = 2.2$; γ -ray luminosity function from Ref. [8]; $\mathcal{L}_{\min} = 10^{42} \text{erg s}^{-1}$; fiducial relation $M(\mathcal{L})$ determined from Ref. [70], see Sec. 3.2.2 for details.
mAGN	Misaligned Active Galactic Nuclei: power-law energy spectrum with $\alpha_{\text{mAGN}} = 2.37$; γ -ray luminosity function from Ref. [9]; see Sec. 3.2.3 for the $M(\mathcal{L})$ relation.
SFG	Star forming galaxies: power-law energy spectrum with $\alpha_{\text{SFG}} = 2.7$; γ -ray luminosity function from Ref. [12]; see Sec. 3.2.4 for the $M(\mathcal{L})$ relation.

Table 1. Summary of the names and characteristics of the considered γ -ray emitter classes.

emitters considered in this paper and it provides a summary of their main characteristics.

4 The tomographic-spectral approach

In Paper I, we proposed for the first time the study of the cross-correlation between cosmic shear and γ -ray anisotropies. We demonstrated that the signal is within reach, when combining weak lensing surveys such as DES and *Euclid* with γ -ray data from the Fermi-LAT satellite. In the present analysis, we elaborate on that idea by determining to what extent the measurement of such a cross-correlation is able to detect a DM signature, and possibly to reconstruct the properties of the DM particle, for instance its mass and γ -ray production rate, either through annihilations or decays.

To this aim, we exploit the whole information available from both kinds of experiments. The redshift measurements performed by weak lensing surveys allow us to subdivide the cosmic shear signal into redshift bins, a procedure usually referred to as ‘redshift tomography’ [79]. Similarly, measuring the energy of the γ rays also allows for a binning in energy. We call this a ‘tomographic-spectral’ approach. We split the gravitational lensing signal into N_z redshift bins, computing N_z window functions W^{κ_i} , each of them defined as the integral of Eq. (2.8) over the i -th redshift bin. In the same way, the energy range is binned in N_E energy intervals—each of them corresponding to a window function W^{γ_a} obtained by integrating Eqs (2.3), (2.5) and (2.6) over in the proper energy range. We define the cross-correlation

tomographic-spectral matrix $\mathbf{C}_\ell^{\gamma\kappa}$ as

$$\mathbf{C}_\ell^{\gamma\kappa} = \begin{pmatrix} C_\ell^{\gamma 1 \kappa 1} & \dots & C_\ell^{\gamma 1 \kappa N_z} \\ \vdots & \ddots & \vdots \\ C_\ell^{\gamma N_E \kappa 1} & \dots & C_\ell^{\gamma N_E \kappa N_z} \end{pmatrix}, \quad (4.1)$$

where each element $C_\ell^{\gamma a \kappa i}$ is the cross-correlation APS obtained from Eq. (3.16) with the window functions $W^{\kappa i}$ and $W^{\gamma a}$, i.e. within i -th redshift bin and the a -th energy bin. Similarly, the auto-correlation matrices $\mathbf{C}_\ell^{\gamma\gamma}$ and $\mathbf{C}_\ell^{\kappa\kappa}$ can be constructed for the γ -ray emission and the cosmic shear signal, respectively. Note that $\mathbf{C}_\ell^{\gamma\gamma}$ and $\mathbf{C}_\ell^{\kappa\kappa}$ are square matrices, whilst $\mathbf{C}_\ell^{\gamma\kappa}$ is a $N_E \times N_z$ object.

4.1 Survey specifications

In order to estimate the auto- and cross-correlation APS and to assess properly the sensitivity to a DM signal, we need to define the characteristics of the detectors. As in Paper I, we focus on DES [33] and *Euclid* [34, 35], considered as representatives of current and future cosmic shear surveys. The former is a ground-based experiment provided with an extremely sensitive 570-Megapixel digital camera mounted on the Blanco 4 m telescope at Cerro Tololo Inter-American Observatory high in the Chilean Andes. It started taking data in September 2012 and it will continue for 5 years, surveying 5,000 square degrees over the Southern sky. On the other hand, *Euclid* is a European Space Agency space-based, medium-class astronomy and astrophysics mission, whose launch is planned for 2020. *Euclid* will observe 15,000 deg² of the darkest sky that is free of contamination by light from our Galaxy and the Solar System. Its weak lensing survey will measure several billion photometric redshifts of galaxies as far as $z \gtrsim 2$.

The expected source redshift distribution for DES can be written as

$$\frac{dN_g^{\text{DES}}}{dz}(z) \propto \frac{z^a + z^{ab}}{z^b + c}, \quad (4.2)$$

with $a = 0.612$, $b = 8.125$ and $c = 0.62$ [80]. For *Euclid*, the source distribution has the form [81]

$$\frac{dN_g^{\text{Euclid}}}{dz}(z) \propto z^2 \exp \left[- (z/z_0)^{1.5} \right], \quad (4.3)$$

where $z_0 = z_m/1.41$ and $z_m = 0.9$ is the median redshift of the survey.

We report in Table 2 the details of our modelling of the surveys and of the redshift binning. For the case of DES, we follow Ref. [82] and we take 3 equally-spaced bins between $z = 0.3$ and $z = 1.5$. For *Euclid*, we adopt the specifications for the weak-lensing photometric survey, suggesting 10 bins between $0 < z < 2.5$ with photometric scatter $\sigma_z = 0.03(1 + z)$. Note that, according to recent estimates, a more realistic value of $\sigma_z/(1 + z)$ should be 0.05. However, we checked that this does not strongly influence our results.

Fermi-LAT is the principal scientific instrument on the Fermi Gamma Ray Space Telescope spacecraft, launched into a near-Earth orbit in June 2008. The design life of the mission is 5 years and the goal for mission operations is 10 years. Fermi-LAT is an imaging high-energy γ -ray telescope covering the energy range from about 20 MeV to more than 300 GeV. Its field of view covers about 20% of the sky at any time, and in survey mode it scan the whole sky every three hours. An exposure of 5 years (after analysis cuts) represents our

Parameter	Description	DES	<i>Euclid</i>
f_{sky}	Surveyed sky fraction	0.12	0.36
$\bar{N}_g [\text{arcmin}^{-2}]$	Galaxy density	13.3	30
$dN_g/dz(z)$	Redshift distribution	Ref. [80]	Ref. [81]
$z_{\text{min}} - z_{\text{max}}$	Redshift range	0.3 – 1.5	0 – 2.5
N_z	Number of bins	3	10
Δ_z	Bin width	0.4	0.25
$\sigma_z/(1+z)$	Redshift uncertainty	–	0.03
σ_ϵ	Intrinsic ellipticity	0.3	0.3

Table 2. Summary of the specifications for DES and *Euclid*.

Parameter	Description	<i>Fermi-5yr</i>	<i>Fermi-10yr</i>	<i>‘Fermissimo’</i>
f_{sky}	Surveyed sky fraction	1	1	1
$E_{\text{min}} - E_{\text{max}} [\text{GeV}]$	Energy range	1 – 300	1 – 300	0.3 – 1000
N_E	Number of bins	6	6	8
$\varepsilon [\text{cm}^2 \text{ s}]$	Exposure	1.6×10^{12}	3.2×10^{12}	4.2×10^{12}
$\langle \sigma_b \rangle [\text{deg}]$	Average beam size	0.18	0.18	0.027

Table 3. Summary of the different configurations assumed for the γ -ray experiments. We mention here that, in reality, the analysis will not be full sky (e.g., the plane is typically cut out), but the fraction of γ -ray sky considered will still remain significantly larger than the ones of the galaxy surveys in Table 2, which thus set the f_{sky} for the cross-correlation.

benchmark configuration, that we will refer to as *Fermi-5yr*. However, we will also consider an exposure of 10 years, a scenario that we call *Fermi-10yr*. Finally, we also consider a hypothetical upgrade (dubbed *‘Fermissimo’*) as a representative case of a future space-based large-area full-sky γ -ray detector, with improved capabilities with respect to Fermi-LAT. Proposals currently under study include Gamma400 [83], HERD [84] and DAMPE [85]. We do not specifically assume any of these designs, but we take inspiration from them in defining the characteristics of *‘Fermissimo’*.

Table 3 summarises the main experimental characteristics of the three experimental configurations. We consider 6 energy bins for *Fermi-5yr* and *Fermi-10yr* (specifically, 1–2 GeV, 2–5 GeV, 5–10 GeV, 10–50 GeV, 50–100 GeV and 100–300 GeV) and we add one additional bin at lower energies (between 0.3 and 1 GeV) and one at higher energies (between 300 GeV and 1 TeV) for *‘Fermissimo’*. The energy resolution of the detector is significantly smaller than the bin width, namely $\Delta E/E \lesssim 20\%$. However, considering bins that are too small implies a reduced statistics, with no consequent gain in information. In Table 3, we also present the properties of the assumed γ -ray campaigns. Note that we quote the average beam size $\langle \sigma_b \rangle$ but, in the following, we adopt the values taken from Ref. [86], allowing σ_b to change with the energy; for example, the angular resolution of Fermi-LAT reaches 0.1 deg at high energies.

Now that we have fixed the experimental setup, in Fig. 8 we show the elements of the tomographic-spectral matrices for the DES+*Fermi-5yr* configuration. The top panel shows the γ -ray auto-correlation APS $C_\ell^{\gamma^a \gamma^b}$, the middle panel the auto-correlation APS of cosmic shear $C_\ell^{\kappa_i \kappa_j}$ and the cross-correlation APS $C_\ell^{\gamma^a \kappa_j}$ is plotted in the bottom panel. For the auto-correlation APS (top and middle panels) solid curves refer to the diagonal elements (the auto-correlation APS obtained considering the same energy or redshift bin), whilst dashed

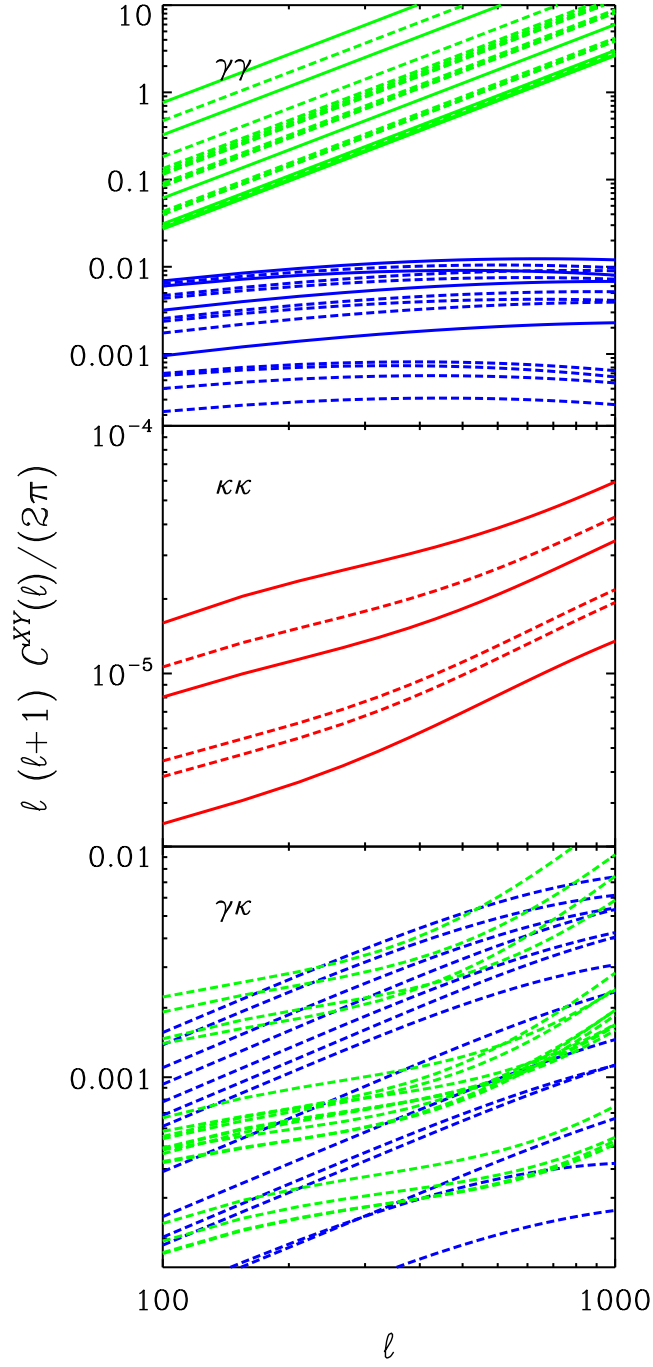


Figure 8. Tomographic-spectral matrix elements $\mathbf{C}_\ell^{\gamma\gamma}$ (top panel), $\mathbf{C}_\ell^{\kappa\kappa}$ (middle panel) and $\mathbf{C}_\ell^{\gamma\kappa}$ (bottom panel), for annihilating DM (blue), astrophysical background (green) and cosmic shear (red). Each curve corresponds to one element of the matrices. Solid lines refer to diagonal entries and dashed lines to off-diagonal ones. The plots refer to the HIGH substructure scheme and to the combination of DES and *Fermi-5yr* data.

curves are for off-diagonal terms. Blue lines refer to the case in which annihilating DM (in the

HIGH scenario) is responsible for the γ -ray emission, whilst, for green lines, the γ -ray emission is due to the sum of all the astrophysical sources considered before. Without entering into details for all curves, the main purpose of this graph is to show that the cross-correlation of γ -ray anisotropies and cosmic shear provides a powerful way to get rid of the overwhelming astrophysical background (as proved also in Fig. 5 of Paper I). Indeed, although astrophysical sources largely dominate the auto-correlation signal (top panel), the cross-correlation spectra for astrophysical and DM sources span the same orders of magnitude (bottom panel). This makes the cross-correlation a more promising strategy for DM investigation, compared to γ -ray auto-correlation.

5 Analysis technique

In this section we estimate the potentiality of the cross-correlation technique to uncover a DM signal. We will proceed in two ways: *i*) for each of DM mass m_{DM} we determine the minimal $\langle\sigma_a v\rangle$ and Γ_d with which the cross-correlation signal provides a detection of the DM particle with a confidence level (CL) larger than 5σ ; and *ii*) we investigate the precision that can be achieved by the various experimental setups in the reconstruction of the particle DM parameters (i.e. its mass and annihilation cross section or decay rate) for a set of representative benchmark cases.

The technique we employ to forecast the prospects for detection is the Bayesian Fisher matrix method. The technique will be discussed in the following section, whilst the results will be presented in Sec. 6.

5.1 Fisher matrix fundamentals

The Fisher matrix approach for parameter estimation assumes the presence of a likelihood function $L(\boldsymbol{\vartheta})$ that quantifies the agreement between a certain set of experimental data and the set of parameters of the model, $\boldsymbol{\vartheta} = \{\vartheta_\alpha\}$. It is also assumed that the behaviour of the likelihood near its maximum characterises the whole likelihood function sufficiently well to be used to estimate errors on the model parameters [87–89].

Under the hypothesis of a Gaussian likelihood (hyper)surface, the Fisher matrix is defined as the inverse of the covariance matrix. Thence, it is possible to infer the statistical accuracy with which the data encoded in the likelihood can measure the parameters $\boldsymbol{\vartheta}$. If the data is taken as expected measurements performed by future experiments, the Fisher matrix method can be used, as we do here, to determine their prospects for detection and the viable level of accuracy. The 1σ marginal error on parameter ϑ_α reads

$$\sigma(\vartheta_\alpha) = \sqrt{(\mathbf{F}^{-1})_{\alpha\alpha}}, \quad (5.1)$$

where \mathbf{F}^{-1} is the inverse of the Fisher matrix, and no summation over equal indices is applied here.

Our experimental data will come from the measurement of the cross-correlation APS C_ℓ^{XY} between the observables X and Y , as discussed in the previous section. More specifically, we will use the cross-correlation tomographic-spectral matrix $\mathbf{C}_\ell^{\gamma\kappa}$ defined in Sec. 4. The parameters $\boldsymbol{\vartheta}$ in our model are $\{m_{\text{DM}}, \Gamma_d, \mathcal{A}_{\text{BLA}}, \mathcal{A}_{\text{SFG}}, \mathcal{A}_{\text{mAGN}}\}$ for decaying DM and $\{m_{\text{DM}}, \langle\sigma_a v\rangle, \mathcal{A}_{\text{BLA}}, \mathcal{A}_{\text{SFG}}, \mathcal{A}_{\text{mAGN}}\}$ for annihilating DM. Unless stated otherwise, we fix the annihilation/decay energy spectrum to be that produced by the hadronisation of b quarks. We also fix the description of astrophysical sources to the model discussed in Sec. 2.2, leaving

only the quantities \mathcal{A}_{BLA} , \mathcal{A}_{SFG} and $\mathcal{A}_{\text{mAGN}}$ as free parameters. We remind the reader that these quantities quantify the deviation from our fiducial case in the normalisation of the 1-halo term of the 3D cross-correlation PS of blazars, SFGs and mAGNs, respectively.

Following Ref. [90], the generic element of the covariance matrix $\mathbf{\Gamma}_{\ell\ell'}^{\gamma\kappa}$ can be expressed as

$$[\mathbf{\Gamma}_{\ell\ell'}^{\gamma\kappa}]^{ai,bj} = \frac{\widehat{C}_{\ell}^{\gamma_a\kappa_j}\widehat{C}_{\ell}^{\gamma_b\kappa_i} + \widehat{C}_{\ell}^{\gamma_a\gamma_b}\widehat{C}_{\ell}^{\kappa_i\kappa_j}}{(2\ell+1)\Delta\ell f_{\text{sky}}}\delta_K^{\ell\ell'}, \quad (5.2)$$

where $\Delta\ell$ is the bin width (for angular multipole binned data), f_{sky} is the fraction of sky probed by the survey, and δ_K is the Kronecker symbol. Here, $\widehat{\mathbf{C}}_{\ell}^{XY} = \mathbf{C}_{\ell}^{XY} + \mathcal{N}_{\ell}^{XY}$, being \mathcal{N}_{ℓ}^{XY} the experimental noise on the measurement of \mathbf{C}_{ℓ}^{XY} . We assume that noises for γ rays and cosmic shear do not correlate, so that $\mathcal{N}_{\ell}^{\gamma\kappa} = 0$. This also implies $\widehat{\mathbf{C}}_{\ell}^{\gamma\kappa} = \mathbf{C}_{\ell}^{\gamma\kappa}$. Conversely, for the auto-correlation terms we have

$$\mathcal{N}_{\ell}^{\gamma_a\gamma_b} = \delta_K^{ab} \frac{4\pi f_{\text{sky}}}{\bar{N}_{\gamma_a}} \mathcal{W}_{\ell}^{-2}, \quad (5.3)$$

$$\mathcal{N}_{\ell}^{\kappa_i\kappa_j} = \delta_K^{ij} \frac{\sigma_{\epsilon}^2}{\bar{N}_{g_i}}, \quad (5.4)$$

where the first term describes the so-called photon noise and \bar{N}_{γ_a} is the total number of γ rays expected in the a -th energy bin. The factor $\mathcal{W}_{\ell} = \exp(-\sigma_b^2 \ell^2/2)$ is the window of a Gaussian point-spread function and \bar{N}_{g_i} is the number of galaxies per steradian in the i -th redshift bin.

Now, it is worth to make a remark. We emphasise that our method consists in a cross-correlation between two distinct signal. For a start—as we stated above—this implies that $\mathcal{N}_{\ell}^{\gamma\kappa} = 0$, because cosmic-shear and γ -ray noises do not correlate. However, this has besides another major advantage, which is the fact that any *additive* systematic effect shall not correlate either. Thus, this method is more robust than a simple auto-correlation analysis.⁴

From an observational viewpoint, we can consider each single mode $\widehat{C}_{\ell}^{\gamma_a\kappa_j}$ in tomographic, spectral and multipole space as a parameter of the theory. Then, to recast the Fisher matrix in the space of the model parameters $\boldsymbol{\vartheta}$, it is sufficient to multiply the inverse of the covariance matrix by the Jacobian of the change of variables, viz.

$$\mathbf{F}_{\alpha\beta} = \sum_{\ell,\ell'=\ell_{\min}}^{\ell_{\max}} \frac{\partial \mathbf{C}_{\ell}^{\gamma\kappa}}{\partial \vartheta_{\alpha}} [\mathbf{\Gamma}_{\ell\ell'}^{\gamma\kappa}]^{-1} \frac{\partial \mathbf{C}_{\ell'}^{\gamma\kappa}}{\partial \vartheta_{\beta}}, \quad (5.5)$$

where we sum over all the multipoles because $\mathbf{\Gamma}_{\ell\ell'}^{\gamma\kappa}$ is diagonal in ℓ and ℓ' .

We characterise the potential of the cross-correlation technique in terms of two analyses. First, in order to determine the minimal $\langle\sigma_a v\rangle$ and Γ_d that correspond to a 5σ DM detection, we construct the Fisher matrix given in Eq. (5.5) by varying over the full set of parameters $\boldsymbol{\vartheta}$. Astrophysical parameters \mathcal{A}_i will be marginalised over, whilst the DM parameters m_{DM} and $\langle\sigma_a v\rangle$ or Γ_d will be retained. For each value of DM mass, we determine the value for $\langle\sigma_a v\rangle$ or Γ_d that is 5 times larger than its estimated error computed from Eq. (5.1). This corresponds to the minimal $\langle\sigma_a v\rangle$ or Γ_d above which it will be possible to discriminate between an interpretation of the cross-correlation data in terms of astrophysics only and an

⁴Nonetheless, note that other, non-additive systematics may have an impact, such as shape bias in the case of cosmic shear.

interpretation that requires a DM component. We refer to this situation as a *DM detection* with a 5σ CL. Notice that, when obtaining the 5σ CL detection, we do not assume a specific fiducial model for the DM particle but leave the DM parameters free to vary over suitable ranges. We call this first analysis the determination of the *detection reach* of the cross-correlation technique, and its results will be presented in Sec. 6.1.

As a second step, we forecast the precision that can be achieved in the reconstruction of the particle DM parameters. To do this we assume a few benchmark DM models by fixing m_{DM} , $\langle\sigma_a v\rangle$ and Γ_d . We derive the 1σ and 2σ marginal errors with which those quantities can be determined from the cross-correlation measurement according to the marginal error of Eq. (5.1). As before, the astrophysical parameters \mathcal{A}_i are marginalised over. We refer to this analysis as *parameter estimation*, and its results will be presented in Sec. 6.2.

As stated above, we consider DES and *Euclid* as representative experiments for the weak lensing data, and Fermi-LAT (with two different exposures, relative to 5 and 10 years of data) as our γ -ray detector. We also take into account the hypothetical future γ -ray detector ‘*Fermissimo*’. We report our results for three distinct combinations, corresponding to increasing sensitivities and, possibly, available on increasingly longer timescales. These are: *i*) DES+*Fermi-5yr*, a situation which is experimentally attainable in the very next future; *ii*) *Euclid*+*Fermi-10yr*, available not earlier than mid 2020s; and *iii*) *Euclid*+‘*Fermissimo*’ for a scenario even further in the future.

6 Results

6.1 Detection reach

We start by discussing the case of annihilating DM. The lines in Fig. 9 mark the region in the $(m_{\text{DM}}, \langle\sigma_a v\rangle)$ -plane above which the cross-correlation provides a 5σ detection of the DM particle. Here, we refer to the DES+*Fermi-5yr* combination, a situation that can be achieved possibly within 2015-2016. The results are obtained after the marginalisation over the \mathcal{A}_i amplitudes of the astrophysical sources. The range considered for \mathcal{A}_{BLA} is between 0.05 and 50, for \mathcal{A}_{SFG} between 0.1 and 10 and for $\mathcal{A}_{\text{mAGN}}$ between 0.2 and 2. Assuming the HIGH model (blue line), results show that a 5σ detection is possible for a particle with a thermal annihilation cross section of $3 \times 10^{-26} \text{ cm}^3\text{s}^{-1}$, if the m_{DM} is smaller than 300 GeV. In the more conservative case of the LOW subhalo model, the results moves up by an order of magnitude (red line), whilst for the NS case the green line is above $10^{-24} \text{ cm}^3\text{s}^{-1}$. Note that the NS scenario is very conservative and quite unphysical in assuming that no DM structures are present below $M_{\text{min}} = 10^7 M_{\odot}$. It also represents a *guaranteed* DM component that would be unrealistic to neglect (within the WIMP framework).

Fig. 10 shows the impact of different assumptions on the astrophysical components. The three solid lines refer to three fiducial astrophysical models: *i*) a maximal contribution from astrophysics (upper curve), for which all the \mathcal{A}_i fiducial values are fixed to the maximal value allowed, i.e. $\mathcal{A}_{\text{BLA}} = 50$, $\mathcal{A}_{\text{SFG}} = 10$ and $\mathcal{A}_{\text{mAGN}} = 2$; *ii*) the case in which all the fiducial \mathcal{A}_i are set to 1; and *iii*) a minimal contribution, where the fiducial \mathcal{A}_i ’s hold fixed to their minimum, namely $\mathcal{A}_{\text{BLA}} = 0.05$, $\mathcal{A}_{\text{SFG}} = 0.1$ and $\mathcal{A}_{\text{mAGN}} = 0.2$. Note that, when we estimate the error of the annihilation cross-section through the Fisher matrix, we still marginalise over the values of three \mathcal{A}_i ’s. As discussed in the previous section, the uncertainty on the astrophysical component can be a limiting factor. Indeed, for a maximal astrophysical component, we need a $\langle\sigma_a v\rangle$ that is almost a factor of 10 larger than our fiducial model, in order to have a 5σ detection—at least for massive DM candidates. The difference

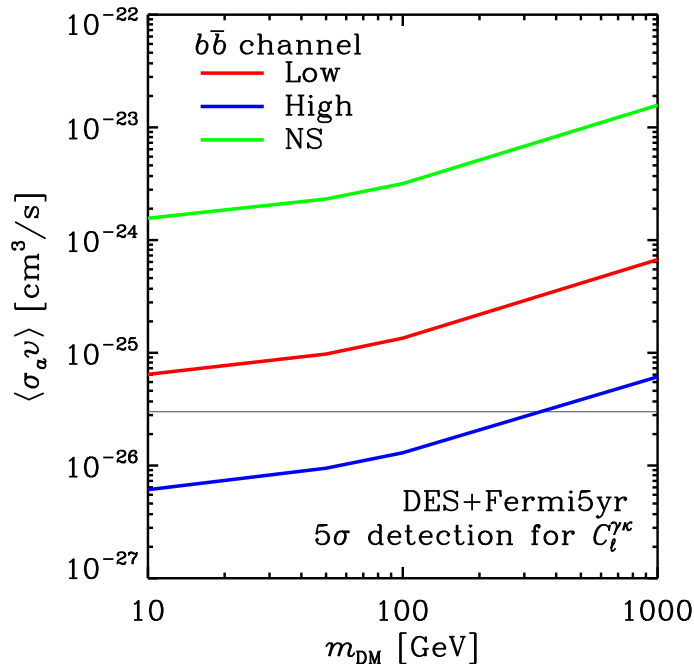


Figure 9. The coloured lines determine the region above which the cross-correlation APS between cosmic shear and γ -ray emission provides a 5σ detection of the DM particle. A 100% branching ratio into b quarks is assumed. The three coloured lines refer to different clustering models (the green line for NS, the red one for LOW and the blue one for HIGH), see Sec. 2.1.1 for more details. The γ -ray emission from astrophysical sources is included in the computation of the cross-correlation signal. Results refer to the combination of DES and *Fermi-5yr* data. The thin grey line indicates the thermal cross section, $3 \times 10^{-26} \text{ cm}^3 \text{ s}^{-1}$.

goes down to a factor of 2 for masses ~ 10 GeV. However, we note that the fiducial case where all normalisations \mathcal{A}_i are set to their maximal value is quite unlikely, since it refers to a model where each γ -ray component has a normalisation systematically 1–2 orders of magnitude larger than the benchmark case. On the contrary, reducing the astrophysical component does not significantly impact on our predictions. This is because, as noted in Fig. 7a, the astrophysical 1-halo terms start to be important at relatively large ℓ 's.

Fig. 10 also shows the impact of the details on how the marginalisation is performed: for each set of curves, dashed lines refer to the case in which the \mathcal{A}_i are thoroughly free to vary allowing for the possibility of them to become arbitrarily large, whilst for the solid lines the \mathcal{A}_i are forced to remain within the prior range mentioned above. The difference between the solid and dashed lines is very small. This reflects the fact that the intervals adopted for the \mathcal{A} factors are very generous. We also mention that Fig. 10 is obtained for the HIGH case, but similar conclusions can be drawn for the other two scenarios.

Figs 9 and 10 illustrate the minimal cross section for which a cross-correlation signal corresponds to a 5σ detection of the DM particle. In the case a signal is not detected, it is customary to derive upper bounds on the annihilation rate as a function of the DM mass. Fig. 11 shows the expected 2σ upper limits that can be obtained from the cross-correlation between γ -ray emission and cosmic shear. Within the Fisher matrix formalism, forecast can be computed only assuming a fiducial model. The upper limits on the annihilation

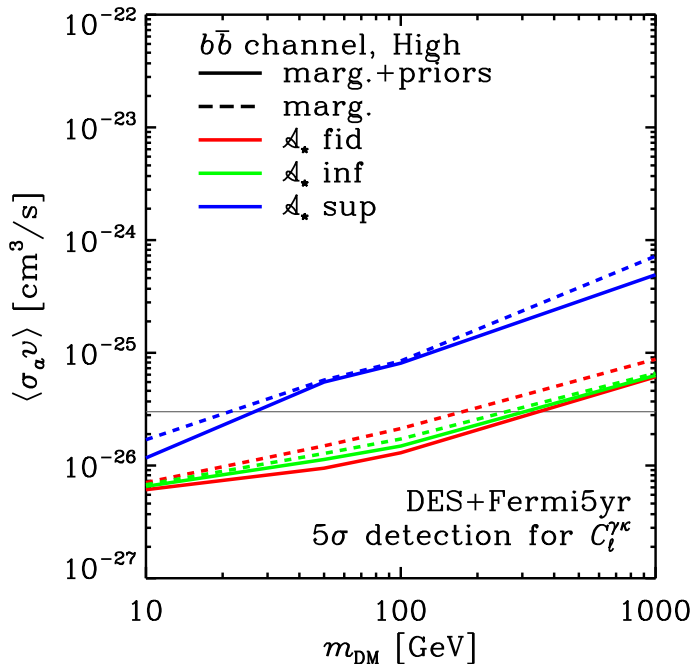


Figure 10. The coloured lines determine the region above which the cross-correlation APS between cosmic shear and γ -ray emission provides a 5σ detection of the DM particle. A 100% branching ratio into b quarks is assumed. The three coloured lines refer to different fiducial models for the astrophysical components (see text for details). For each colour, the solid curve refers to the case in which the marginalisation is performed over the range quoted in the text, whilst for the dashed one we only require \mathcal{A}_i to be positive. Results refer to the combination of DES and *Fermi-5yr* data. The HIGH scenario is assumed. The thin grey line indicates the thermal cross section, $3 \times 10^{-26} \text{ cm}^3 \text{ s}^{-1}$.

rate are thus obtained from the Fisher matrix of Eq. (5.5) with a DM fiducial model with $\langle\sigma_a v\rangle = 0$. In Fig. 11 these limits (solid lines) are compared to the 2σ upper bounds yielded by including only the data from the γ -ray auto-correlation APS [25] (long-dashed lines) or from the EGB intensity [54] (short-dashed lines). These limits are obtained from a similar analysis à la Fisher, but using public data, thus without the need of a fiducial model. The figure refers again to the DES+*Fermi-5yr* case. Blue, red and green lines correspond to the HIGH, LOW and NS scenario, respectively. It is worth noting that, regardless of the clustering scenario assumed, the analysis of the cross-correlation provides upper limits which are a factor of ~ 5 more constraining than those from the intensity alone, and more than a factor of 10 tighter than those derived from auto-correlation APS. As explained in Paper I and in Secs 2 and 4, the information provided by the cross-correlation with the cosmic shear manages to isolate the DM signal in the EGB, even when the EGB intensity and its auto-correlation APS are dominated by astrophysical sources. In turn, this arises from the fact that the window functions of DM-induced emission and of astrophysical sources have quite different behaviours. In particular, DM preferably emits at low redshifts, whilst the astrophysical components peak at a larger redshift (see Fig. 1a). This information is lost when measuring the EGB intensity alone (either as total emission, or through the auto-correlation of its anisotropies), but it can be recovered by cross-correlating it with cosmic shear. In addition, the importance of the 1-halo term and the predicted shape of the APS

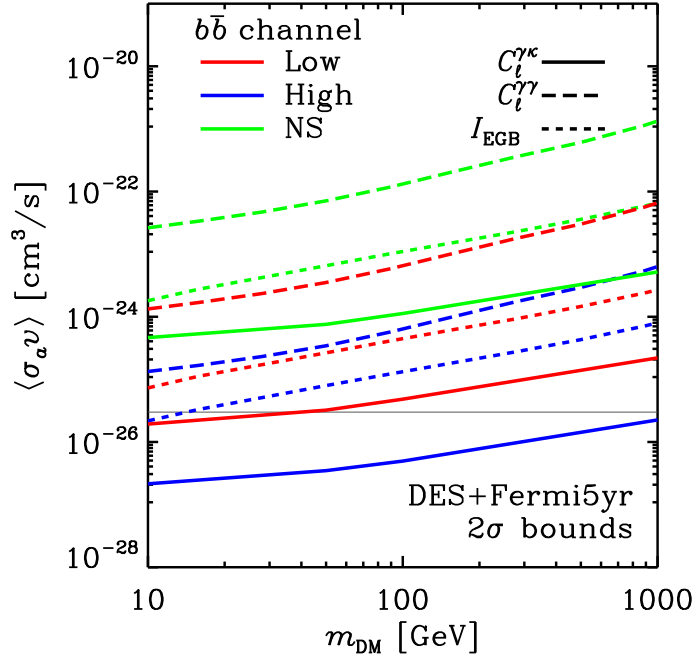


Figure 11. Solid lines show the 2σ upper limits that can be derived from a non-detection of DM from the analysis of the cross-correlation APS between cosmic shear and γ -ray emission. Long- or short-dashed lines provide the same information but in the case of a non-detection from the auto-correlation APS or intensity energy spectrum of the EGB. A 100% branching ratio into b quarks is assumed. The three colours refer to different models for the clustering: blue (red) for HIGH (LOW) and green for the NS model. Results refer to the combination of DES and *Fermi-5yr* data. The thin grey line indicates the thermal cross section, $3 \times 10^{-26} \text{ cm}^3 \text{ s}^{-1}$.

are different between the case of DM-induced and astrophysical emission. This provides an extra piece of information that is lost when averaging over the sky.

The combination of DES and *Fermi-5yr* data-sets is already promising for the detection of DM. To scrutinise what can be achieved by future detectors, Fig. 12 also depicts the prospects for the 5σ detection reach of the combination of *Euclid* and *Fermi-10yr* (central panel) and of *Euclid* and ‘*Fermissimo*’ (right panel). These are compared with the case of DES and *Fermi-5yr* (left panel). The plots are based on the HIGH clustering model. Going from DES+*Fermi-5yr* to *Euclid*+*Fermi-10yr*, there is an improvement of a factor ~ 5 and (for annihilation into b quarks) thermal cross sections will correspond to a DM detection over the whole mass range until 1 TeV. By including the information provided by ‘*Fermissimo*’, it is possible to go down by more than an additional factor 2, thus starting to probe cross sections as low as $5 \times 10^{-28} \text{ cm}^3 \text{ s}^{-1}$ for masses of the order of 10 GeV.

In Fig. 12, we also see the rôle of the annihilation channel. The red lines represent annihilations into b quarks, whilst green lines are for the production of muons and blue lines for τ leptons. This last possibility corresponds to the most promising scenario, always slightly below the case of b quarks. On the other hand, annihilations into muons require the largest cross sections (approximately a factor 4 larger than with b quarks), so that only the *Euclid*+‘*Fermissimo*’ case can probe the thermal cross section in the entire mass range. Let us also note that for masses larger than the TeV, inverse Compton scattering on the CMB due

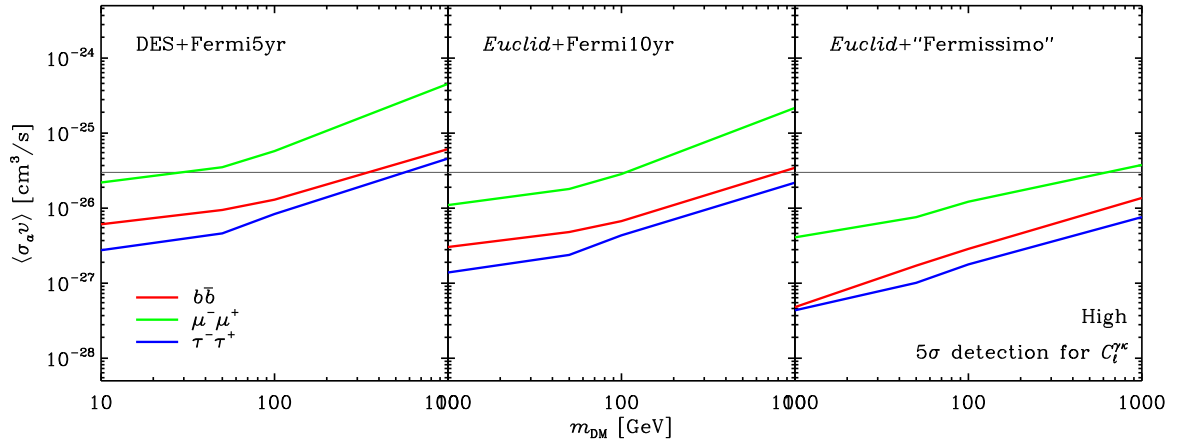


Figure 12. The coloured lines determine the region above which the cross-correlation APS between cosmic shear and γ -ray emission provides a 5σ detection of the DM particle. The predictions refer to the case of DES and *Fermi-5yr* (left panel), *Euclid* and *Fermi-10yr* (central panel) and *Euclid* and ‘*Fermissimo*’ (right panel). In each panel, from top to bottom, the lines refer to the $\mu^+\mu^-$ (green), $b\bar{b}$ (red) and $\tau^+\tau^-$ (blue) annihilation channels. The HIGH scenario is assumed. The thin grey line indicates the thermal cross section, $3 \times 10^{-26} \text{ cm}^3 \text{ s}^{-1}$.

to the electrons produced by the muon decays (here neglected for simplicity as mentioned in Sec. 2.1.1) can increase the γ -ray emission for this channel and therefore improve the detection reach in the high-mass range.

By adopting the HIGH subhalo scenario, Fig. 12 represents the most optimistic case. For the LOW scenario, all curves have otherwise to be raised by approximately one order of magnitude (see Fig. 9). All values spanned between these two scenarios can be considered representative of the uncertainty arising from the clustering modeling. This implies that, also for the LOW case, the combination of *Euclid* and ‘*Fermissimo*’ allows for a high-significance detection for a DM particle with a thermal cross section up to a few hundred GeV for all the annihilation channels—except muons.

6.2 Parameter estimation

We now turn to the discussion of the prospects of the different experimental setups for the reconstruction of the DM particle physics parameters. We consider a set of representative benchmark cases: for annihilating DM we take 3 values of DM masses ($m_{\text{DM}} = 10, 100, 1000$ GeV) and a common value for the annihilation cross section, viz. $\langle\sigma_a v\rangle = 3 \times 10^{-26} \text{ cm}^3 \text{ s}^{-1}$. For decaying DM, the masses considered are $m_{\text{DM}} = 20, 200, 2000$ GeV (to give the same energy end-points in the γ -ray spectra as in the case of annihilation), and a representative value $\Gamma_d = 0.33 \times 10^{-27} \text{ s}^{-1}$ for the decay rate, corresponding to a decay lifetime $\tau_d = 3 \times 10^{27} \text{ s}$.

We start by considering an annihilating DM candidate, and Fig. 13 (left panel) shows the forecasts for the reconstruction of the DM properties achieved with the combination of DES and *Fermi-5yr* for the $b\bar{b}$ annihilation channel and the HIGH clustering model. The filled areas and empty contours refer 1σ and 2σ marginal errors, respectively. As in the previous section, we marginalise over the \mathcal{A}_i factors. We notice that the tomographic-spectral approach has the potential of resolving a DM signal and of measuring its DM properties over a wide range of masses. The two lighter benchmarks enable us to perform a more accurate reconstruction,

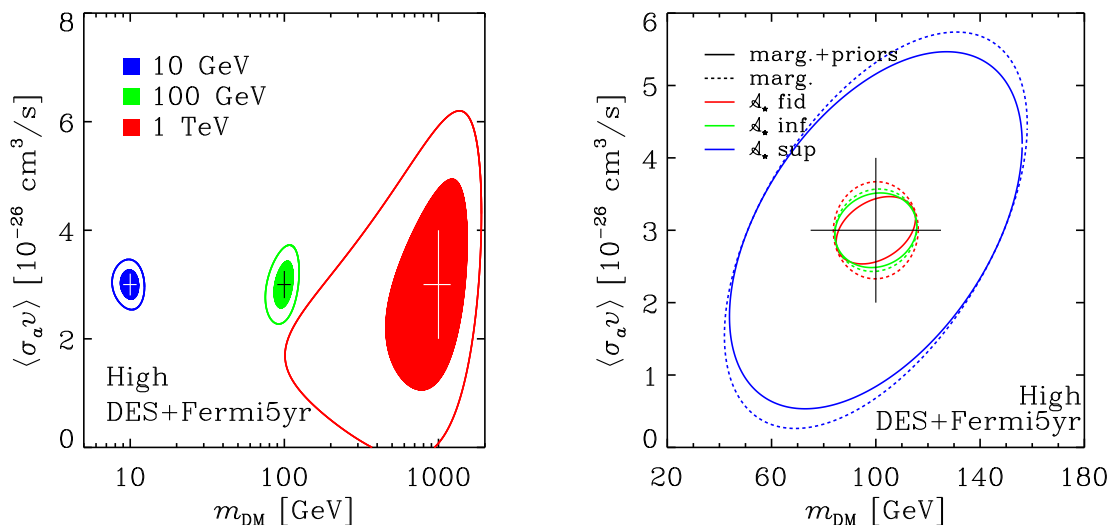


Figure 13. Forecasts for the reconstruction of the DM mass and annihilation cross section, achieved by the combination of DES and *Fermi-5yr*, for the $b\bar{b}$ annihilation channel and the HIGH clustering subhalo model. Results are for a cross section of $\langle\sigma_a v\rangle = 3 \times 10^{-26} \text{ cm}^3 \text{ s}^{-1}$. Left: The three benchmark DM models have masses of 10 GeV (blue), 100 GeV (green) and 1 TeV (red), from left to right. Filled areas and empty contours refer to the 1σ and 2σ CL reconstruction, respectively. Right: The three coloured lines refer to different fiducial models for the astrophysical components (see text for details). For each colour, the solid curve refers to the case in which the marginalisation is performed over the range quoted in the text, whilst for the dashed one we only require \mathcal{A}_i to be positive. A benchmark DM model with a mass of 100 GeV is chosen. The contours refer to the 1σ CL reconstruction.

with both mass and cross section reconstructed with a precision better than a factor of 2. This is because lighter DM particles imply larger γ -ray fluxes, as can be seen in Eq. (2.3), as a consequence of the dependence of the signal on the particle number density squared, namely $n^2 = \rho^2 m_{\text{DM}}^{-2}$. Moreover, the spectral information plays a very important rôle in the reconstruction of the DM mass (see also Fig. 14b and the discussion later in this section). For the 10 and 100 GeV mass benchmarks, the end-point of the DM-induced γ -ray spectrum is located within the energy range considered in our analysis (i.e. between 1 and 300 GeV) and it is thus easier to discriminate a DM-induced energy spectrum from the featureless power-laws characterising astrophysical sources. On the other hand, this is not the case for the benchmark at $m_{\text{DM}} = 1 \text{ TeV}$.

The impact of the modelling of the astrophysical sources is considered in Fig. 13 (right panel), where the 1σ contours for the benchmark model with a mass of 100 GeV are reported (under the same assumption of left panel, namely a $b\bar{b}$ annihilation channel, DES+*Fermi-5yr* data and HIGH clustering model). However, as done in Fig. 10, each set of ellipses refer to a different fiducial astrophysical source model. Blue ellipses stand for a maximal astrophysical component, where all \mathcal{A}_i normalisations are set to their maximal allowed value (i.e. $\mathcal{A}_{\text{BLA}} = 50$, $\mathcal{A}_{\text{SFG}} = 10$ and $\mathcal{A}_{\text{mAGN}} = 2$); red ellipses are for when all fiducial \mathcal{A}_i are set to 1; and green contours show the case in which astrophysical sources contribute at their minimum (i.e. $\mathcal{A}_{\text{BLA}} = 0.05$, $\mathcal{A}_{\text{SFG}} = 0.1$ and $\mathcal{A}_{\text{mAGN}} = 0.2$). The uncertainties on both the DM mass and annihilation rate are of the order of 60% when the astrophysical background components are maximal, and of 20% for the fiducial background model. The case with

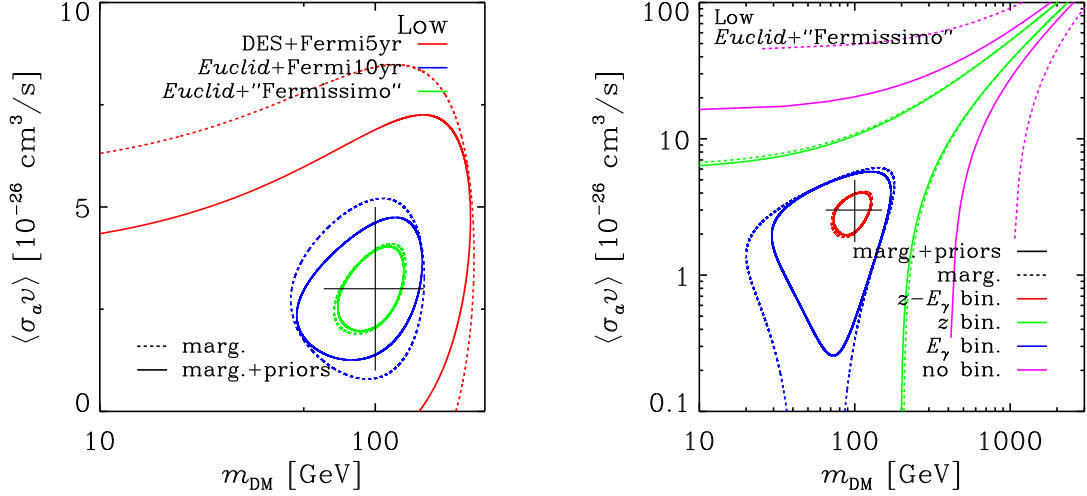


Figure 14. Forecasts for the reconstruction of DM mass and annihilation cross section, for a DM particle with a mass of 100 GeV, thermal annihilation cross section and $b\bar{b}$ annihilation channel. The LOW clustering model is assumed. Contours show the 1σ CL reconstruction. Left: Red contours refer to data provided by the combination of DES and *Fermi-5yr* whilst blue (green) regions corresponds to the combination of *Euclid* and *Fermi-10yr* (*‘Fermissimo’*). For each set of curves, solid lines correspond to marginalisation of the parameters \mathcal{A}_i over the range mentioned in the text, whilst dashed line are obtained assuming only that $\mathcal{A}_i > 0$. Right: Magenta contours refer to the case in which neither redshift nor energy binning is considered. Green (blue) lines show the case where only the binning in redshift (energy) is considered, whilst for the red contours both are implemented. Solid/dashed coding as for the left panel. The combination of *Euclid* and *‘Fermissimo’* data are assumed.

minimal astrophysical is very similar to the red contours. Even if the results are obtained from the benchmark with $m_{\text{DM}} = 100$ GeV, similar results hold true also over a wide areas of the DM parameter space, including larger masses and cross sections below the thermal value (as it can be expected by looking at Fig. 12).

In Fig. 13b we also see the effect of marginalisation over the priors. Dashed ellipses refer to the case in which the \mathcal{A}_i are left free over the range mentioned above. On the other hand, a wider range (i.e. $\mathcal{A}_i > 0$) is used for the solid lines. Differences are minimal.

Fig. 14a depicts the improvement that can be achieved by considering future experiments. Results refer again to the benchmark scenario with a mass of 100 GeV and thermal cross section. A conservative LOW clustering scenario is assumed. Red contours are for a combination of DES and *Fermi-5yr* data, whilst blue and green contours respectively refer to the case *Euclid+Fermi-10yr* or *Euclid+‘Fermissimo’*. The impact of considering *Euclid* is dramatic and the experiment will allow for the reconstruction of DM properties within a factor of 2, even with the LOW clustering model. This will be already possible even without a future generation γ -ray detectors beyond Fermi-LAT.

The improvement in the parameter reconstruction shown in Fig. 14a is due to larger statistics and to a finer redshift resolution that enables a finer tomographic slicing for the surveyed redshift ranges (we go from 3 bins for DES to 10 bins for *Euclid*, see Tab. 2). The inclusions of a future γ -ray experiment (green contours) allows for a larger energy range and improved angular resolutions, which is why contours shrink even further.

Fig. 14b proves that the crucial ingredient for the reconstruction of the DM mass comes from considering the spectral information, as it was suggested above. Results are presented for the same benchmark model of left panel and considering data coming from *Euclid* and ‘*Fermissimo*’. Magenta contours refer to the case in which no binning is considered in the analysis of the cross-correlation data, neither in redshift nor in energy. In this case, the reconstruction is affected by a strong degeneracy between mass and cross section. Indeed, in this case, the cross-correlation is simply constraining the strength of the DM component and, given Eq. (2.3) which depends on the quantity $S = \langle \sigma_a v \rangle m_{\text{DM}}^{-2} \int_{E_{\text{min}}}^{E_{\text{max}}} dN_a/dE_\gamma$, where $E_{\text{max}} = m_{\text{DM}}$ if m_{DM} is smaller than the maximal detector energy $E_{\text{max}}^{\text{det}}$ (which in our analysis for *Euclid*+‘*Fermissimo*’ is 1 TeV, see Table 3). This implies that the cross-correlation is constraining the quantity $S \sim \langle \sigma_a v \rangle / m_{\text{DM}}$ (or $S \sim \langle \sigma_a v \rangle E_{\text{max}}^{\text{det}} / m_{\text{DM}}^2$), giving rise to the degeneracy between mass and annihilation cross section.

When the binning in z is performed (green contours), tomography significantly shrinks the contour sizes, thus illustrating that integrating in redshift up to 2.5 (see Table 2), as done for the magenta contours, dilutes the discrimination power. However, it is still not enough to close the 1σ contour, since no new independent piece of information is provided on the mass or the cross section. On the other hand, if we only include the binning in energy (blue contours), the spectral information allows for the cross-correlation to determine closed contours in the reconstruction of both m_{DM} and $\langle \sigma_a v \rangle$. As we commented before, this comes from the fact that the DM-induced γ -ray spectrum is quite different from astrophysical spectra, which are typically simple power laws. Finally, including also the binning in redshift enables the full exploitation of the complementarity between the spectral and tomographic information. The red contours are now closed and very tight, corresponding to a good reconstruction of the DM properties with a precision smaller than a factor of 2.

Notice that, whenever a contour includes the case with $\langle \sigma_a v \rangle = 0$ (i.e. ‘open’ ellipse), this implies that the technique just is able to provide an upper limit on the annihilation cross section. This is because, in order to derive the contours, we employ the Fisher formalism, computing the derivatives in Eq. (5.5) at the fiducial m_{DM} and $\langle \sigma_a v \rangle$. A Gaussian likelihood is assumed, but this approximation clearly breaks down when $\langle \sigma_a v \rangle$ goes to zero. Therefore when an ellipse includes $\langle \sigma_a v \rangle = 0$, only the upper part should be considered (as the corresponding upper limit), while the lower part of the ellipse has no physical meaning. For example, the lower edge of the solid pink contour in Fig. 14, going rapidly to zero in the range $m_{\text{DM}} = 300 - 500$ GeV, should not be considered.

In Fig. 15, we show how our forecasts depend upon the annihilation channel. Results are shown for a DM particle with a mass of 100 GeV and a thermal cross section. The LOW scenario and data from *Euclid* and ‘*Fermissimo*’ are assumed. The red area represents the case of a $b\bar{b}$ annihilation channel (as considered in the previous figures), whilst blue and green regions stand for $\tau^+\tau^-$ and $\mu^+\mu^-$ annihilation channels, respectively. The figure shows that the assumption on the annihilation channel has a large impact on the reconstruction capability of the cross-correlation.

The size of the contours is mostly set by efficiency of the channel in producing photons. A larger photon yield (as for the $b\bar{b}$ and $\tau^+\tau^-$ cases) increases the sensitivity of the cross-correlation technique (see also Fig. 12) and in turn the capability of reconstructing mass and annihilation rate. The case of muons as final states produces a lower amount of photons and is hence the one with the worst forecast (contours are not closed in the region plotted of Fig. 15). Another aspect to be taken into account is that different channels have different spectral shapes and some of them can mimic the astrophysical emission, thus making the

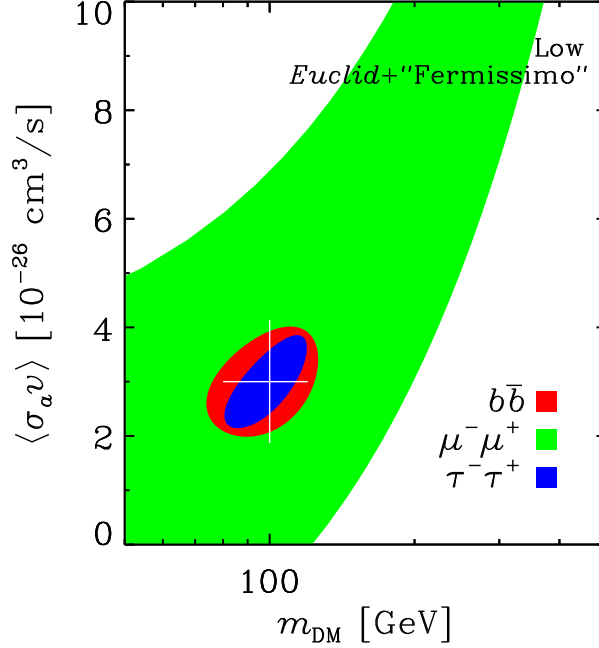


Figure 15. Forecasts for the reconstruction of the DM mass and annihilation cross section, for a DM particle with a mass of 100 GeV and thermal annihilation cross section. The LOW clustering model and the combination of *Euclid* and ‘*Fermissimo*’ are assumed. The red, green and blue contours respectively refer to the case of annihilations into b quarks, τ s and $\mu^+\mu^-$. The contours show the 1σ CL reconstruction.

reconstruction of the DM signal more difficult. This has however less impact than the emitted photon multiplicity.

We now consider the case of a decaying DM candidate, computing the precision that can be achieved by the γ -ray and cosmic-shear cross-correlation in the reconstruction of its mass, m_{DM} , and decay rate, Γ_d . In Fig. 16a, we show the contours for the three benchmarks considered here: a particle with a mass of 20 GeV, 200 GeV and 2 TeV (blue, green and red contours, respectively). The decay rate is fixed at a common value of $\Gamma_d = 0.33 \times 10^{-27} \text{ s}^{-1}$. The analysis refers to the combination of *Euclid* and ‘*Fermissimo*’. Analogously to the case of annihilating DM, the reconstruction power is extremely good. Both the mass and the decay rate can be potentially determined with a high level of accuracy.

Fig. 16b depicts the impact of binning in redshift and energy, for a benchmark case at $m_{\text{DM}} = 200 \text{ GeV}$. We notice that also here the spectral information is crucial in the reconstruction of the DM mass. The same comments of Fig. 14b apply here, with the notable difference that in the case of decay, Eq. (2.5) shows that the signal has a different dependence on the DM mass: $S = \Gamma_d m_{\text{DM}}^{-1} \int_{E_{\text{min}}}^{E_{\text{max}}} dN_a/dE_\gamma$. This implies that whenever $m_{\text{DM}} < E_{\text{max}}^{\text{det}}/2$ ($E_{\text{max}}^{\text{det}} = 1 \text{ TeV}$, in the case of Fig. 16), the signal behaves as $S \sim \Gamma_d$, with no relevant dependence on the DM mass. This explains the flat behavior of the contours in Fig. 16b for low DM masses. Otherwise, when $m_{\text{DM}} > E_{\text{max}}^{\text{det}}/2$, the signal roughly scales as $S \sim \Gamma_d E_{\text{max}}^{\text{det}}/m_{\text{DM}}$, which explains the turn up of the contours. This argument also explains why the reconstruction capabilities (shown in the left panel) are similar at different DM masses. For smaller masses, the sensitivity is lost due to the fact that most of the produced

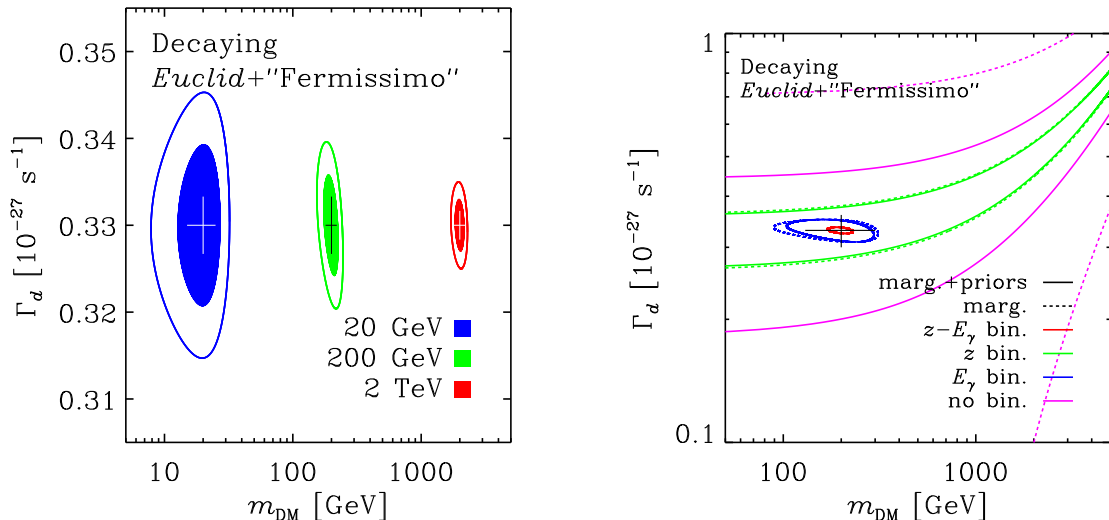


Figure 16. Forecasts for the reconstruction of the DM mass and the decay rate, for a DM particle with a decay rate of $\Gamma_d = 0.33 \times 10^{-27} \text{ s}^{-1}$ and decay channel into b quarks. Results refer to the combination of data from *Euclid* and ‘*Fermisismo*’. Left: Forecasts for three benchmark masses, 20 GeV (blue contours), 200 GeV (green contours) and 2 TeV (red contours). The full (empty) contours refer to the 1σ (2σ) CL reconstruction. Right: Forecasts for a DM particle with a mass of 200 GeV. The magenta contours refer to the case in which no binning is considered, neither in redshift nor in energy. Green (blue) curves show the case where only the binning in redshift (energy) is considered, whilst for the red contours both are implemented. The contours show the 1σ CL reconstruction. For each set of lines, solid lines consider marginalisation of the parameters \mathcal{A}_i over the range mentioned in the text, whilst dashed lines are obtained assuming $\mathcal{A}_i > 0$.

photons fall below the detector threshold, which we fix at 300 MeV for ‘*Fermisismo*’.

To summarise the results on the capability of reconstructing DM properties with the cross-correlation expected from *Euclid* and ‘*Fermisismo*’, we report in Table 4 the 1σ marginal errors for three benchmark models in the case of annihilating DM (leftmost columns) and decaying DM (rightmost columns). A $b\bar{b}$ spectrum is assumed, together with the LOW clustering scenario. As usual, the astrophysical components are marginalised over. In the annihilating case, the benchmark refers to the thermal cross-sections. In this case, we see that both m_{DM} and $\langle\sigma_a v\rangle$ can be reconstructed with an uncertainty smaller than 20% up to DM masses of the order of 100 GeV, while the reconstruction capabilities degrade for DM masses at the TeV scale. In the decaying DM case, the relative uncertainties, on the contrary, reduce at large masses, as already noticed in Fig. 16a.

7 Conclusions

In this work we provide realistic prospects for the detection of DM in the cross-correlation between the extra-galactic γ -ray background (EGB) and the weak-lensing signal of cosmic shear. The idea was originally proposed in Paper I [2]. Here, the concept is further investigated by adopting a tomographic-spectral approach. We also improve our modelling of the EGB, in particular of its astrophysical components. Unresolved astrophysical sources contribute to the EGB and they represent a background that has to be properly modelled

m_{DM} [GeV]	$\langle\sigma_a v\rangle$ [10^{-26} cm ³ s ⁻¹]	m_{DM} [GeV]	Γ_d [10^{-27} s ⁻¹]
10 ± 0.53	3 ± 0.20	20 ± 4.9	0.33 ± 0.062
100 ± 18	3 ± 0.68	200 ± 19	0.33 ± 0.039
1000 ± 951	3 ± 3.7	2000 ± 119	0.33 ± 0.020

Table 4. Forecast 1σ marginal errors for the three benchmark models of DM considered here. The leftmost columns are for annihilating DM particles, whilst the rightmost ones for decaying DM particles. Results are for a $b\bar{b}$ channel and a LOW subhalo model. They refer to the data provided by a combination of *Euclid* and ‘*Fermissimo*’. All \mathcal{A}_i parameters encoding the normalisation of the astrophysical components are marginalised over.

and understood in order to have access to the DM component. Our description of the EGB includes the contributions from unresolved blazars, misaligned AGNs (mAGNs) and star forming galaxies (SFGs), alongside with γ rays induced by DM annihilations or decays. For each astrophysical population, we discuss an important ingredient for the computation of their correlation with the lensing signal, i.e. the relation between the γ -ray luminosity of a source and the mass of the host DM halo $M(\mathcal{L})$. We find that such a relation is quite unknown but it has only a moderate impact on the prospects for the detection of DM.

We discuss how the uncertainties related to the clustering of DM at low masses affect the cross-correlation signal. In particular, we focus on the dependence of the signal on the value of minimal halo mass M_{min} and on the amount of subhaloes.

Finally, we adopt the Fisher matrix approach to derive forecast for a combination of current and future detectors including Fermi-LAT, DES, *Euclid* and a unspecified future γ -ray detector called ‘*Fermissimo*’. We determine the minimum annihilation cross section or decay rate that allows us to detect a DM particle from the measurement of the cross-correlation signal, and estimate the precision in the reconstruction of the DM properties (its mass, annihilation and decay rate) that can be reached by analysing the data of those experiments through the technique of cross-correlation.

The main conclusions of this paper can be summarised as follows:

- The γ -ray emission expected from mAGNs and SFGs can contribute significantly to the cross-correlation signal and they represent an important background for the detection of DM (see Fig. 7a). In the most optimistic scenario for annihilating DM (HIGH), the cross-correlation induced by DM is comparable in intensity to that produced by astrophysical γ -ray emission (see Fig. 8). However, this is not enough to compromise the detection of a DM signal (see later). We note also that this case would produce a subdominant (negligible) contribution to the total EGB (γ -ray auto-correlation APS). In the future, the discovery of new SFGs and mAGNs will improve our understanding of these populations, facilitating even more the reconstruction of the DM component.
- The intensity of the DM component to the cross-correlation depends on the way DM clusters at low masses. Predictions can vary over two orders of magnitude, as it can be seen in Figs. 3a and 8. We note that similar uncertainties affect the EGB induced by DM.
- In the case of annihilating DM, the measurement of the cross-correlation in the data from DES and *Fermi-5yr* has the potential to detect a DM particle with an annihilation cross section smaller than the thermal value of 3×10^{-26} cm³s⁻¹, for a DM mass smaller than 300 GeV. This result refers to the HIGH subhalo scenario, whilst predicted signal

reduces by a factor of ~ 10 for the more conservative LOW scenario, and by a further factor of 20 for the more pessimistic case named NS (see Fig. 9). We note that this last possibility is quite unlikely but it corresponds to a guaranteed signal that cannot be neglected.

- The prospects for detection significantly improve with the inclusion of *Euclid* data. Indeed, for the combination of *Euclid* and ‘*Fermissimo*’, a thermal annihilation cross section will correspond to a DM detection over the whole range of masses considered here (10 GeV to 1 TeV) and for all annihilation channels (apart from a small region with $m_{\text{DM}} > 600$ GeV for annihilations into muons, see Fig. 12), in the HIGH scenario. With this experimental setup, cross sections as low as $5 \times 10^{-28} \text{ cm}^3 \text{ s}^{-1}$ are still able to provide a detection of DM, at least for masses of the order of 10 GeV.
- The power of the proposed technique comes from the combination of the three independence sources of information: *i)* the different redshift scaling between astrophysical and DM components (see Fig. 1a); *ii)* the different energy spectrum (see Fig. 1b); and *iii)* the fact that the DM signal is dominated by the largest DM haloes (producing a large gravitational lensing effect) whilst the astrophysical sources considered here are normally hosted in smaller structures with $M \ll 10^{14} M_{\odot}$. The tomographic-spectral approach provides an excellent sensitivity to DM even when such a component is only subdominant in intensity or in the auto-correlation APS.
- In the case of lack of a DM detection (i.e. the cross-correlation is found to be compatible with the astrophysical components only), the measurement can be used to derive 2σ limits on the annihilation cross section (see Fig. 11). The upper limits achievable for the HIGH case are more stringent than the 95% CL limits obtained from the observation of the dwarf spheroidal galaxies performed by Fermi-LAT [91] and from the observation of the Galactic halo from H.E.S.S. [92]. These limits represent, at the moment, the strongest constraints on annihilating DM. Fig. 11 shows how a measurement of the cross-correlation signal, potentially available on a timescale of 1–2 years, could become already competitive with long-standing strategies for the indirect detection of DM. Even in the unlikely NS scenario, the green line would be more constraining than what has been achieved to date by Imaging Cherenkov Telescopes from the observation of dwarf spheroidals (see e.g. Ref. [93]).
- When used to reconstruct the properties of the DM particle, the cross-correlation can yield very precise results. If the DM is a particle with properties similar to a canonical WIMP (i.e., mass around 100 GeV and annihilation rate of the order of $3 \times 10^{-26} \text{ cm}^3 \text{ s}^{-1}$), m_{DM} and $\langle \sigma_a v \rangle$ can be reconstructed at the 20–30% level for a combination of data from DES and *Fermi-5yr* in the HIGH clustering scenario (see Fig. 13) and *Euclid* and ‘*Fermissimo*’ in the LOW scenario (see Fig. 14 and Table 4).
- Similar conclusions apply to the decaying DM case. However, when compared other Galactic probes, the extragalactic signal from decaying DM is less promising than in the case of annihilating DM. Indeed, the latter signal scales with ρ_{DM}^2 and can acquire a large boost factor from big structures in the Universe (possibly hosting a large amount of substructures). This fact can significantly enhance the reach of extragalactic signatures with respect to the Galactic ones, while it does not happen in the decaying DM scenario which scales linearly with ρ_{DM} .

In conclusion, the cross-correlation between cosmic shear and diffuse γ -ray emission represents a very powerful mean of investigation for particle DM. A cross-correlation signal robustly interpreted in terms of DM would establish DM as a particle, against alternative interpretations based on modifications of Einstein’s general relativity [2]. Such a measurement would also allow us to reconstruct the properties of the DM particle (e.g. its mass and annihilation or decay rate) to a good level of precision for a relevant fraction of its parameter space.

Acknowledgments

SC is funded by FCT-Portugal under Post-Doctoral Grant SFRH/BPD/80274/2011. MF gratefully acknowledges support of the Leverhulme Trust and of the project MultiDark CSD2009-00064. This work is also supported by the research grant *Theoretical Astroparticle Physics* number 2012CPPYP7 under the program PRIN 2012 funded by the Ministero dell’Istruzione, Università e della Ricerca (MIUR), by the research grants *TAsP (Theoretical Astroparticle Physics)* and *Fermi* funded by the Istituto Nazionale di Fisica Nucleare (INFN), and by the *Strategic Research Grant: Origin and Detection of Galactic and Extragalactic Cosmic Rays* funded by the University of Torino and Compagnia di San Paolo.

A The $M(\mathcal{L})$ relation for misaligned Active Galactic Nuclei

In Sec. 3.2.3, the γ -ray luminosity of mAGNs has been related to the mass M_\bullet of the SMBH at the center of the AGN, exploiting the fact that both are correlated to the core radio luminosity $L_{r,\text{core}}$. However, this procedure results in estimates for M_\bullet that are too large (see dashed blue line in Fig. 17a). Moreover, the link between M_\bullet and $L_{r,\text{core}}$ is not completely well-established (see Refs. [43, 73]). Therefore, we decide to consider also an alternative approach, based on the information available in the literature about the mAGNs detected by Fermi-LAT. Among the 15 mAGNs discussed in Ref. [9], we found measurements for the central SMBH for 12 of them. More precisely: see Ref. [73] for NGC 1218, Cen A, 3C 120, PKS-0625-35, 3C 84, Ref. [94] for NGC 1218, 3C 120, 3C 380, 3C 84, NGC 1275, Ref. [95] for NGC 1218, NGC 1275, Ref. [75] for M 87, Ref. [96] for Cen A, Ref. [97] for For A, Ref. [98] for 3C 111 and Ref. [99] for IC 310. When more than one measurement is available for the same object, we consider the average and we also sum the error in quadrature. If the resulting error is smaller than 50% of SMBH mass, we artificially increase it to 50% of M_\bullet , in order to be conservative. The masses, estimated in this way, are coupled to the γ -ray luminosity taken from Ref. [9] and the 12 data points are plotted in Fig. 17a. The solid red lines shows the result of a fit assuming a power law relation between the two quantities.

Finally, the relation between the mass of the SMBH and the host DM halo is taken from Ref. [70] (which inherits it from Ref. [74]). However, we normalise it in order to pass through the point ($M_\bullet = 6.6 \times 10^9 M_\odot$, $M = 2.2 \times 10^{13} M_\odot$) [75, 76], corresponding to the case of M 87.

This relation combined with the power law fit of $M_\bullet(\mathcal{L})$ (red curve in the left panel) gives the solid red line in Fig. 17b. The dashed black line shows how the relation would look like without the renormalisation to the case of M 87.

For 4 mAGNs we also find estimates for the mass of the DM halo. Specifically we consider Ref. [76] for M 87, Refs [100, 101] for Cen A, Ref. [102] for For A and Ref. [103]

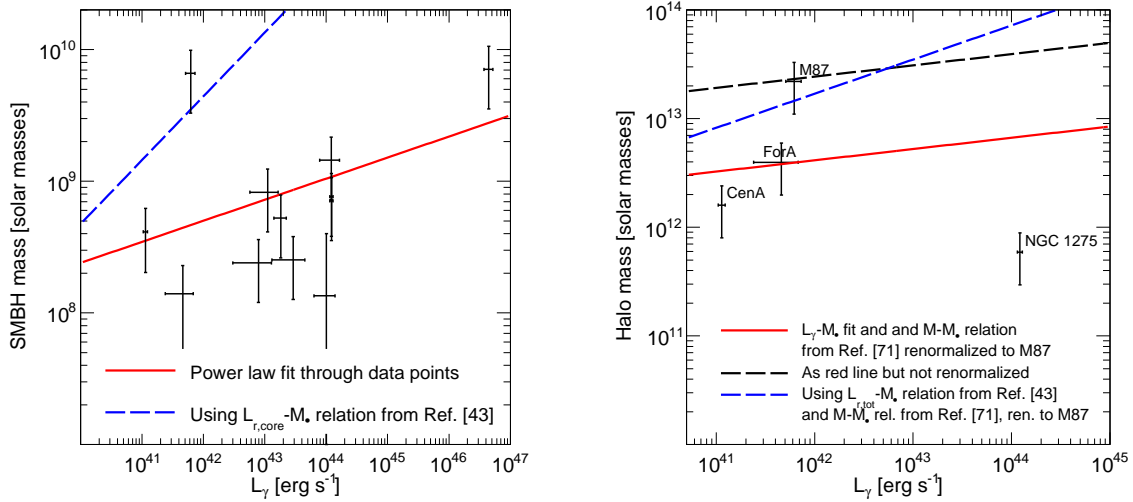


Figure 17. Left: SMBH mass as a function of γ -ray luminosity. The 12 data points correspond to the 12 MAGNs from the sample analyzed in Ref. [9] for which it was possible to find measurement of the mass of their central SMBH M_\bullet (see text for details). The latter is plotted against the γ -ray luminosity \mathcal{L} between 0.1 and 100 GeV taken from Ref. [9]. The solid red line shows the result of a power law fit to the data. The dashed blue line indicates the $M_\bullet - \mathcal{L}$ relation obtained by exploiting the correlation of the two quantities with $L_{r,\text{core}}$ (following Ref. [43]). Right: Halo mass as a function of γ -ray luminosity. The solid red line is obtained by combining the fit to the data in the left panel with the $M_\bullet - M$ relation from Ref. [70], renormalised to reproduce the properties of M 87. The dashed black line shows how the red line would look like without renormalising the $M_\bullet - M$ correlation to the case of M 87. The dashed blue line presents the $M(\mathcal{L})$ obtained by using the $L_{r,\text{core}} - M_\bullet$ relation from Ref. [43] (see blue dashed line in left panel) together with the $M_\bullet - M$ relation from Ref. [70] renormalised to M 87. The 4 data points correspond to the only 4 mAGNs in Ref. [9] for which it was possible to find estimates of the mass of their DM haloes. See text for details and references.

for NGC 1275⁵. For Cen A, two values are available and we consider the average of the two. The error in the DM halo mass is taken to be 50% of the estimated mass. These data for these 4 mAGNs are plotted in Fig. 17b, together with their γ -ray luminosity from Ref. [9].

Despite having too few points to derive firm conclusions, we note that the data are not located far away from the solid red line, while well below the dashed blue line. The latter shows the $M(\mathcal{L})$ obtained by combining the $M - M_\bullet$ relation from Ref. [70] (renormalised to reproduce the properties of M 87) and the $L_{r,\text{core}} - M_\bullet$ relation from Ref. [43] (see blue dashed line in the left panel). This represents our benchmark $M(\mathcal{L})$ relation employed in the rest of the paper. We note that it may over-estimate the halo mass, although it should be kept in mind that the four data-points considered might be not representative. A large value for the mass of the host DM halo would correspond to a generous 1-halo term in the 3-dimensional power spectrum and, thus, a conservative estimate of how the cross-correlation of mAGNs may compete with a DM signal.

⁵For NGC 1275, Ref. [103] only provides an estimate of the stellar mass. We estimate the DM halo mass by assuming a value of 0.05 for the ratio between stellar and DM mass.

B The $M(\mathcal{L})$ relation for star-forming galaxies

In Sec. 3.2.4, the mass of the DM halo hosting a SFG is derived from its γ -ray luminosity via the determination of its SFR. Here, we discuss how to derive the $M(\mathcal{L})$ empirically, based on the few SFGs detected by Fermi-LAT for which we could find measurements for the mass of their DM halo. In particular, we consider the MW from Ref. [104] and M31 from Ref. [105]. For SMC, NGC 253, NGC 1068 and NGC 4945 we refer to the rotation curves in Refs [106, 107]. These are fitted by a simple model with a DM halo and a disk, leaving the normalisations of the two components free, as well as the scale radius of the DM halo and the scale radius of the disk (4 parameters). The fit is performed excluding the first radial bins (corresponding to the inner region) in order to be independent on possible structures (e.g. bulges or bars) in the very center of the galaxies.

Fig. 18 present the estimated masses for the DM haloes. The solid thick blue line also shows the result of a power law fit to the data and it gives the desired $M(\mathcal{L})$ relation. The thin solid blue lines indicates a reasonable uncertainty band that encompass the data points considered. We also show the predictions obtained implementing the M –SFR from Ref. [78] (Model III) and relating the SFR to \mathcal{L} as found in Ref. [12]. The solid red line is obtained with the parameters of Model III fixed to their average value. To estimate the uncertainty band, we left the two main parameters of their description (i.e α_0 and ϵ , see Ref. [78] for their definition) free to vary. For the thin dashed red lines we take ϵ within its 95% confidence level region, leaving α_0 to its average value. For the thin red solid lines we also vary α_0 to the values corresponding to its 95% confidence level.

References

- [1] **Planck Collaboration** Collaboration, P. Ade *et. al.*, *Planck 2013 results. XVI. Cosmological parameters*, [arXiv:1303.5076](#).
- [2] S. Camera, M. Fornasa, N. Fornengo, and M. Regis, *A Novel Approach in the Weakly Interacting Massive Particle Quest: Cross-correlation of Gamma-Ray Anisotropies and Cosmic Shear*, *Astrophys.J.* **771** (2013) L5, [[arXiv:1212.5018](#)].
- [3] **The Fermi LAT collaboration** Collaboration, M. Ackermann *et. al.*, *The spectrum of isotropic diffuse gamma-ray emission between 100 MeV and 820 GeV*, [arXiv:1410.3696](#).
- [4] Y. Inoue and T. Totani, *The Blazar Sequence and the Cosmic Gamma-Ray Background Radiation in the Fermi Era*, *Astrophys.J.* **702** (2009) 523–536, [[arXiv:0810.3580](#)].
- [5] K. N. Abazajian, S. Blanchet, and J. P. Harding, *The Contribution of Blazars to the Extragalactic Diffuse Gamma-ray Background and Their Future Spatial Resolution*, *Phys.Rev.* **D84** (2011) 103007, [[arXiv:1012.1247](#)].
- [6] **Fermi-LAT Collaboration** Collaboration, *The Fermi-LAT high-latitude Survey: Source Count Distributions and the Origin of the Extragalactic Diffuse Background*, *Astrophys.J.* **720** (2010) 435–453, [[arXiv:1003.0895](#)].
- [7] M. Ajello, M. Shaw, R. Romani, C. Dermer, L. Costamante, *et. al.*, *The Luminosity Function of Fermi-detected Flat-Spectrum Radio Quasars*, *Astrophys.J.* **751** (2012) 108, [[arXiv:1110.3787](#)].
- [8] J. P. Harding and K. N. Abazajian, *Models of the Contribution of Blazars to the Anisotropy of the Extragalactic Diffuse Gamma-ray Background*, *JCAP* **1211** (2012) 026, [[arXiv:1206.4734](#)].

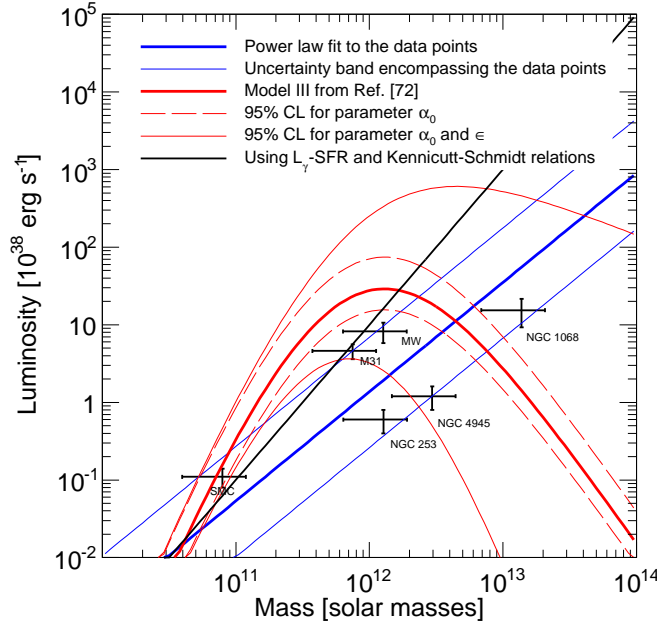


Figure 18. The relation between γ -ray luminosity and the host DM mass for SFGs. The data points are taken from Ref. [12], whilst the measurements of the DM halo mass are derived from literature or from rotation curves (see text for details). The thick solid blue lines indicates the result of a power law fit of the 6 data points. The thin solid blue line show a reasonable uncertainty band, encompassing the data. The red lines show the results implementing the relation between SFR and DM halo mass obtained in Ref. [78] (Model III). See text for details. The solid black line represents the fiducial model adopted in this paper and it is obtained by combining the \mathcal{L} -SFR relation from Ref. [12] and the Kennicutt-Schmidt relation.

- [9] M. Di Mauro, F. Calore, F. Donato, M. Ajello, and L. Latronico, *Diffuse γ -ray emission from misaligned active galactic nuclei*, *Astrophys.J.* **780** (2014) 161, [[arXiv:1304.0908](#)].
- [10] M. Ajello, R. Romani, D. Gasparrini, M. Shaw, J. Bolmer, *et. al.*, *The Cosmic Evolution of Fermi BL Lacertae Objects*, *Astrophys.J.* **780** (2014) 73, [[arXiv:1310.0006](#)].
- [11] Y. Inoue, *Contribution of the Gamma-ray Loud Radio Galaxies Core Emissions to the Cosmic MeV and GeV Gamma-Ray Background Radiation*, *Astrophys.J.* **733** (2011) 66, [[arXiv:1103.3946](#)].
- [12] **Fermi LAT Collaboration** Collaboration, M. Ackermann *et. al.*, *GeV Observations of Star-forming Galaxies with Fermi LAT*, *Astrophys.J.* **755** (2012) 164, [[arXiv:1206.1346](#)].
- [13] B. C. Lacki, S. Horiuchi, and J. F. Beacom, *The Star-Forming Galaxy Contribution to the Cosmic MeV and GeV Gamma-Ray Background*, [[arXiv:1206.0772](#)].
- [14] I. Tamborra, S. Ando, and K. Murase, *Star-forming galaxies as the origin of diffuse high-energy backgrounds: Gamma-ray and neutrino connections, and implications for starburst history*, [[arXiv:1404.1189](#)].
- [15] P. Ullio, L. Bergstrom, J. Edsjo, and C. G. Lacey, *Cosmological dark matter annihilations into gamma-rays - a closer look*, *Phys.Rev.* **D66** (2002) 123502, [[astro-ph/0207125](#)].
- [16] S. Ando and E. Komatsu, *Anisotropy of the cosmic gamma-ray background from dark matter annihilation*, *Phys.Rev.* **D73** (2006) 023521, [[astro-ph/0512217](#)].

- [17] S. Ando, E. Komatsu, T. Narumoto, and T. Totani, *Dark matter annihilation or unresolved astrophysical sources? Anisotropy probe of the origin of cosmic gamma-ray background*, *Phys.Rev.* **D75** (2007) 063519, [[astro-ph/0612467](#)].
- [18] J. M. Siegal-Gaskins, *Revealing dark matter substructure with anisotropies in the diffuse gamma-ray background*, *JCAP* **0810** (2008) 040, [[arXiv:0807.1328](#)].
- [19] J. M. Siegal-Gaskins and V. Pavlidou, *Robust identification of isotropic diffuse gamma rays from Galactic dark matter*, *Phys.Rev.Lett.* **102** (2009) 241301, [[arXiv:0901.3776](#)].
- [20] J. Zavala, V. Springel, and M. Boylan-Kolchin, *Extragalactic gamma-ray background radiation from dark matter annihilation*, *Mon.Not.Roy.Astron.Soc.* **405** (2010) 593, [[arXiv:0908.2428](#)].
- [21] M. Fornasa, L. Pieri, G. Bertone, and E. Branchini, *Anisotropy probe of galactic and extra-galactic Dark Matter annihilations*, *Phys.Rev.* **D80** (2009) 023518, [[arXiv:0901.2921](#)].
- [22] J. Zavala, M. Vogelsberger, T. R. Slatyer, A. Loeb, and V. Springel, *The cosmic X-ray and gamma-ray background from dark matter annihilation*, *Phys.Rev.* **D83** (2011) 123513, [[arXiv:1103.0776](#)].
- [23] M. Fornasa, J. Zavala, M. A. Sanchez-Conde, J. M. Siegal-Gaskins, T. Delahaye, *et. al.*, *Characterization of Dark-Matter-induced anisotropies in the diffuse gamma-ray background*, *MNRAS*, **429**, **1529** (2013) [[arXiv:1207.0502](#)].
- [24] S. Ando and E. Komatsu, *Constraints on the annihilation cross section of dark matter particles from anisotropies in the diffuse gamma-ray background measured with Fermi-LAT*, *Phys.Rev.* **D87** (2013), no. 12 123539, [[arXiv:1301.5901](#)].
- [25] **Fermi LAT Collaboration** Collaboration, M. Ackermann *et. al.*, *Anisotropies in the diffuse gamma-ray background measured by the Fermi LAT*, *Phys.Rev.* **D85** (2012) 083007, [[arXiv:1202.2856](#)].
- [26] A. Cuoco, E. Komatsu, and J. Siegal-Gaskins, *Joint anisotropy and source count constraints on the contribution of blazars to the diffuse gamma-ray background*, *Phys.Rev.* **D86** (2012) 063004, [[arXiv:1202.5309](#)].
- [27] **Collaboration Fermi-LAT** Collaboration, G. Gomez-Vargas *et. al.*, *Dark Matter implications of Fermi-LAT measurement of anisotropies in the diffuse gamma-ray background*, [arXiv:1303.2154](#).
- [28] N. Fornengo and M. Regis, *Particle dark matter searches in the anisotropic sky*, *Front. Physics* **2** (2014) 6, [[arXiv:1312.4835](#)].
- [29] N. Kaiser, *Weak gravitational lensing of distant galaxies*, *Astrophys.J.* **388** (1992) 272.
- [30] M. Bartelmann and P. Schneider, *Weak gravitational lensing*, *Phys.Rept.* **340** (2001) 291–472, [[astro-ph/9912508](#)].
- [31] D. Munshi, P. Valageas, L. Van Waerbeke, and A. Heavens, *Cosmology with Weak Lensing Surveys*, *Phys.Rept.* **462** (2008) 67–121, [[astro-ph/0612667](#)].
- [32] M. Bartelmann, *Gravitational Lensing*, *Class.Quant.Grav.* **27** (2010) 233001, [[arXiv:1010.3829](#)].
- [33] **Dark Energy Survey Collaboration** Collaboration, T. Abbott *et. al.*, *The dark energy survey*, [astro-ph/0510346](#).
- [34] **EUCLID Collaboration** Collaboration, R. Laureijs *et. al.*, *Euclid Definition Study Report*, [arXiv:1110.3193](#).
- [35] **Euclid Theory Working Group** Collaboration, L. Amendola *et. al.*, *Cosmology and fundamental physics with the Euclid satellite*, *Living Rev.Rel.* **16** (2013) 6, [[arXiv:1206.1225](#)].

- [36] M. Shirasaki, S. Horiuchi, and N. Yoshida, *Cross-Correlation of Cosmic Shear and Extragalactic Gamma-ray Background: Constraints on the Dark Matter Annihilation Cross-Section*, [arXiv:1404.5503](#).
- [37] C. Heymans, L. Van Waerbeke, L. Miller, T. Erben, H. Hildebrandt, *et. al.*, *CFHTLenS: The Canada-France-Hawaii Telescope Lensing Survey*, [arXiv:1210.0032](#).
- [38] J.-Q. Xia, A. Cuoco, E. Branchini, M. Fornasa, and M. Viel, *A cross-correlation study of the Fermi-LAT γ -ray diffuse extragalactic signal*, *Mon.Not.Roy.Astron.Soc.* **416** (2011) 2247–2264, [[arXiv:1103.4861](#)].
- [39] S. Ando, A. Benoit-Lvy, and E. Komatsu, *Mapping dark matter in the gamma-ray sky with galaxy catalogs*, *Phys.Rev.* **D90** (2014) 023514, [[arXiv:1312.4403](#)].
- [40] S. Ando, *Power spectrum tomography of dark matter annihilation with local galaxy distribution*, *JCAP* **10** (2014) 061, [[arXiv:1407.8502](#)].
- [41] N. Fornengo, L. Perotto, M. Regis, and S. Camera, *Evidence of cross-correlation between the CMB lensing and the gamma-ray sky*, [arXiv:1410.4997](#).
- [42] T. Sjostrand, S. Mrenna, and P. Z. Skands, *PYTHIA 6.4 Physics and Manual*, *JHEP* **0605** (2006) 026, [[hep-ph/0603175](#)].
- [43] A. Franceschini, G. Rodighiero, and M. Vaccari, *The extragalactic optical-infrared background radiations, their time evolution and the cosmic photon-photon opacity*, *Astron.Astrophys.* **487** (2008) 837, [[arXiv:0805.1841](#)].
- [44] S. Profumo, K. Sigurdson, and M. Kamionkowski, *What mass are the smallest protohalos?*, *Phys.Rev.Lett.* **97** (2006) 031301, [[astro-ph/0603373](#)].
- [45] T. Bringmann, *Particle Models and the Small-Scale Structure of Dark Matter*, *New J.Phys.* **11** (2009) 105027, [[arXiv:0903.0189](#)].
- [46] R. K. Sheth and G. Tormen, *Large scale bias and the peak background split*, *Mon.Not.Roy.Astron.Soc.* **308** (1999) 119, [[astro-ph/9901122](#)].
- [47] J. F. Navarro, C. S. Frenk, and S. D. White, *The Structure of cold dark matter halos*, *Astrophys.J.* **462** (1996) 563–575, [[astro-ph/9508025](#)].
- [48] J. Munoz-Cuartas, A. Maccio, S. Gottlober, and A. Dutton, *The Redshift Evolution of LCDM Halo Parameters: Concentration, Spin, and Shape*, [arXiv:1007.0438](#).
- [49] J. S. Bullock, T. S. Kolatt, Y. Sigad, R. S. Somerville, A. V. Kravtsov, *et. al.*, *Profiles of dark haloes. Evolution, scatter, and environment*, *Mon.Not.Roy.Astron.Soc.* **321** (2001) 559–575, [[astro-ph/9908159](#)].
- [50] M. A. Sanchez-Conde and F. Prada, *The flattening of the concentration-mass relation towards low halo masses and its implications for the annihilation signal boost*, [arXiv:1312.1729](#).
- [51] M. Kamionkowski, S. M. Koushiappas, and M. Kuhlen, *Galactic Substructure and Dark Matter Annihilation in the Milky Way Halo*, *Phys.Rev.* **D81** (2010) 043532, [[arXiv:1001.3144](#)].
- [52] M. A. Sanchez-Conde, M. Cannoni, F. Zandanel, M. E. Gomez, and F. Prada, *Dark matter searches with Cherenkov telescopes: nearby dwarf galaxies or local galaxy clusters?*, *JCAP* **1112** (2011) 011, [[arXiv:1104.3530](#)].
- [53] L. Gao, C. Frenk, A. Jenkins, V. Springel, and S. White, *Where will supersymmetric dark matter first be seen?*, *Mon.Not.Roy.Astron.Soc.* **419** (2012) 1721, [[arXiv:1107.1916](#)].
- [54] **Fermi-LAT collaboration** Collaboration, A. Abdo *et. al.*, *The Spectrum of the Isotropic Diffuse Gamma-Ray Emission Derived From First-Year Fermi Large Area Telescope Data*, *Phys.Rev.Lett.* **104** (2010) 101101, [[arXiv:1002.3603](#)].

- [55] Y. Ueda, M. Akiyama, K. Ohta, and T. Miyaji, *Cosmological evolution of the hard x-ray AGN luminosity function and the origin of the hard x-ray background*, *Astrophys.J.* **598** (2003) 886–908, [[astro-ph/0308140](#)].
- [56] C. J. Willott, S. Rawlings, K. M. Blundell, M. Lacy, and S. A. Eales, *The radio luminosity function from the low-frequency 3crr, 6ce and 7crs complete samples*, *Mon.Not.Roy.Astron.Soc.* **322** (2001) 536–552, [[astro-ph/0010419](#)].
- [57] G. Rodighiero, M. Vaccari, A. Franceschini, L. Tresse, O. L. Fevre, *et. al.*, *Mid- and Far-infrared Luminosity Functions and Galaxy Evolution from Multiwavelength Spitzer Observations up to z 2.5*, [arXiv:0910.5649](#).
- [58] T. Bringmann, F. Calore, M. Di Mauro, and F. Donato, *Constraining dark matter annihilation with the isotropic γ -ray background: updated limits and future potential*, *Phys.Rev.* **D89** (2014) 023012, [[arXiv:1303.3284](#)].
- [59] U. Keshet, E. Waxman, A. Loeb, V. Springel, and L. Hernquist, *Gamma-rays from intergalactic shocks*, *Astrophys.J.* **585** (2003) 128–150, [[astro-ph/0202318](#)].
- [60] **Heidelberg Institute for Theoretical Studies, Heidelberg, Germany** Collaboration, F. Zandanel and F. Prada, *A Phenomenological Model for the Intracluster Medium that matches X-ray and Sunyaev-Zel’dovich observations*, *Mon.Not.Roy.Astron.Soc.* **438** (2014) 116–123, [[arXiv:1311.4793](#)].
- [61] C.-A. Faucher-Giguere and A. Loeb, *The Pulsar Contribution to the Gamma-Ray Background*, *JCAP* **1001** (2010) 005, [[arXiv:0904.3102](#)].
- [62] F. Calore, M. Di Mauro, and F. Donato, *Diffuse gamma-ray emission from galactic Millisecond Pulsars*, [arXiv:1406.2706](#).
- [63] P. S. Coppi and F. A. Aharonian, *Constraints on the VHE emissivity of the universe from the diffuse GeV gamma-ray background*, *Astrophys.J.* **487** (1997) L9–L12, [[astro-ph/9610176](#)].
- [64] M. Ahlers, L. Anchordoqui, M. Gonzalez-Garcia, F. Halzen, and S. Sarkar, *GZK Neutrinos after the Fermi-LAT Diffuse Photon Flux Measurement*, *Astropart.Phys.* **34** (2010) 106–115, [[arXiv:1005.2620](#)].
- [65] N. Kaiser, *Weak lensing and cosmology*, *Astrophys.J.* **498** (1998) 26, [[astro-ph/9610120](#)].
- [66] R. J. Scherrer and E. Bertschinger, *Statistics of primordial density perturbations from discrete seed masses*, *Astrophys.J.* **381** (1991) 349–60.
- [67] D. N. Limber, *The analysis of counts of the extragalactic nebulae of temrs of a fluctuating density field*, *Astrophys.J.* **117** (1953) 134.
- [68] N. Kaiser, *Clustering in real space and in redshift space*, *Mon.Not.Roy.Astron.Soc.* **227** (1987) 1–27.
- [69] A. Cooray and R. K. Sheth, *Halo models of large scale structure*, *Phys.Rept.* **372** (2002) 1–129, [[astro-ph/0206508](#)].
- [70] G. Hutsi, M. Gilfanov, and R. Sunyaev, *Linking X-ray AGN with dark matter halos: a model compatible with AGN luminosity function and large-scale clustering properties*, [arXiv:1304.3717](#).
- [71] S. Ando, E. Komatsu, T. Narumoto, and T. Totani, *Angular power spectrum of gamma-ray sources for GLAST: Blazars and clusters of galaxies*, *Mon.Not.Roy.Astron.Soc.* **376** (2007) 1635–1647, [[astro-ph/0610155](#)].
- [72] A. Franceschini, S. Vercellone, and A. Fabian, *Supermassive black holes in early type galaxies: Relationship with radio emission and constraints on the black hole mass function*, *Mon.Not.Roy.Astron.soc.* (1998) [[astro-ph/9801129](#)].

- [73] D. Bettoni, R. Falomo, G. Fasano, and F. Govoni, *The black hole mass of low redshift radiogalaxies*, *Astron.Astrophys.* **399** (2003) 869–878, [[astro-ph/0212162](#)].
- [74] K. Bandara, D. Crampton, and L. Simard, *A Relationship between Supermassive Black Hole Mass and the Total Gravitational Mass of the Host Galaxy*, *Astrophys.J.* **704** (2009) 1135–1145, [[arXiv:0909.0269](#)].
- [75] K. Gebhardt, J. Adams, D. Richstone, T. R. Lauer, S. Faber, *et. al.*, *The Black-Hole Mass in M87 from Gemini/NIFS Adaptive Optics Observations*, *Astrophys.J.* **729** (2011) 119, [[arXiv:1101.1954](#)].
- [76] K. Gebhardt and J. Thomas, *The Black Hole Mass, Stellar M/L, and Dark Halo in M87*, *Astrophys.J.* **700** (2009) 1690–1701, [[arXiv:0906.1492](#)].
- [77] B. D. Fields, V. Pavlidou, and T. Prodanovic, *Cosmic Gamma-Ray Background from Star-Forming Galaxies*, *Astrophys.J.* **722** (2010) L199, [[arXiv:1003.3647](#)].
- [78] Z. Lu, H. Mo, Y. Lu, N. Katz, M. Weinberg, *et. al.*, *An Empirical Model for the Star Formation History in Dark Matter Halos*, [arXiv:1306.0650](#).
- [79] W. Hu, *Power Spectrum Tomography with Weak Lensing*, *Astrophys. J.* **522** (1999) L21–L24, [[astro-ph/9904153](#)].
- [80] L. Fu, E. Semboloni, H. Hoekstra, M. Kilbinger, L. van Waerbeke, *et. al.*, *Very weak lensing in the CFHTLS Wide: Cosmology from cosmic shear in the linear regime*, *Astron.Astrophys.* **479** (2008) 9–25, [[arXiv:0712.0884](#)].
- [81] I. Smail, R. S. Ellis, and M. J. Fitchett, *Gravitational lensing of distant field galaxies by rich clusters: I. - faint galaxy redshift distributions*, *Mon.Not.Roy.Astron.Soc.* **270** (1994) 245, [[astro-ph/9402048](#)].
- [82] E. Beynon, M. Baldi, D. J. Bacon, K. Koyama, and C. Sabiu, *Weak lensing predictions for coupled dark energy cosmologies at non-linear scales*, *Mon. Not. Roy. Astron. Soc.* **422** (2012) 3546–3553, [[arXiv:1111.6974](#)].
- [83] A. M. Galper, O. Adriani, R. Aptekar, I. Arkhangelskaja, A. Arkhangelskiy, M. Boezio, V. Bonvicini, K. Boyarchuk, M. Fradkin, and Y. Gusakov *et al.*, *Design and Performance of the GAMMA-400 Gamma-Ray Telescope for the Dark Matter Searches*, *American Institute of Physics Conference Series* **1516** (2014) 288–292, [[arXiv:1210.1457](#)].
- [84] **HERD Collaboration** Collaboration, S. Zhang, *The High Energy cosmic-Radiation Detection (HERD) Facility onboard China’s Future Space Station*, [arXiv:1407.4866](#).
- [85] <http://dpnc.unige.ch/dampe/index.html>.
- [86] **LAT Collaboration** Collaboration, W. Atwood *et. al.*, *The Large Area Telescope on the Fermi Gamma-ray Space Telescope Mission*, *Astrophys.J.* **697** (2009) 1071–1102, [[arXiv:0902.1089](#)].
- [87] H. Jeffreys, *Theory of Probability*. 1961. Oxford, UK: Univ. Pr. (1961) 421 p.
- [88] M. S. Vogeley and A. S. Szalay, *Eigenmode analysis of galaxy redshift surveys I. theory and methods*, *Astrophys. J.* **465** (1996) 34–53, [[astro-ph/9601185](#)].
- [89] M. Tegmark, A. Taylor, and A. Heavens, *Karhunen-Loeve eigenvalue problems in cosmology: how should we tackle large data sets?*, *Astrophys. J.* **480** (1997) 22, [[astro-ph/9603021](#)].
- [90] W. Hu and B. Jain, *Joint galaxy - lensing observables and the dark energy*, *Phys. Rev.* **D70** (2004) 043009, [[astro-ph/0312395](#)].
- [91] **Fermi-LAT Collaboration** Collaboration, M. Ackermann *et. al.*, *Dark matter constraints from observations of 25 Milky Way satellite galaxies with the Fermi Large Area Telescope*, *Phys.Rev.* **D89** (2014), no. 4 042001, [[arXiv:1310.0828](#)].

- [92] **H.E.S.S. Collaboration** Collaboration, A. Abramowski *et. al.*, *Search for a Dark Matter annihilation signal from the Galactic Center halo with H.E.S.S.*, *Phys.Rev.Lett.* **106** (2011) 161301, [[arXiv:1103.3266](#)].
- [93] J. Aleksic, S. Ansoldi, L. Antonelli, P. Antoranz, A. Babic, *et. al.*, *Optimized dark matter searches in deep observations of Segue 1 with MAGIC*, *JCAP* **1402** (2014) 008, [[arXiv:1312.1535](#)].
- [94] J.-H. Woo and C. M. Urry, *AGN black hole masses and bolometric luminosities*, *Astrophys.J.* **579** (2002) 530–544, [[astro-ph/0207249](#)].
- [95] H. Falcke, E. Koerding, and S. Markoff, *A Scheme to unify low - power accreting black holes: Jet - dominated accretion flows and the radio / x-ray correlation*, *Astron.Astrophys.* **414** (2004) 895–903, [[astro-ph/0305335](#)].
- [96] N. Neumayer, *The Supermassive Black Hole at the Heart of Centaurus A: Revealed by Gas- and Stellar Kinematics*, [arXiv:1002.0965](#).
- [97] N. Nowak, R. Saglia, J. Thomas, R. Bender, R. Davies, *et. al.*, *The supermassive black hole of Fornax A*, [arXiv:0809.0696](#).
- [98] R. Chatterjee, A. P. Marscher, S. G. Jorstad, A. Markowitz, E. Rivers, *et. al.*, *Connection between the Accretion Disk and Jet in the Radio Galaxy 3C 111*, *Astrophys.J.* **734** (2011) 43, [[arXiv:1104.0663](#)].
- [99] **MAGIC Collaboration** Collaboration, J. Aleksic *et. al.*, *Detection of very high energy gamma-ray emission from the Perseus cluster head-tail galaxy IC 310 by the MAGIC telescopes*, *Astrophys.J.* (2010) [[arXiv:1009.2155](#)].
- [100] K. A. Woodley, W. E. Harris, M. A. Beasley, E. W. Peng, T. J. Bridges, *et. al.*, *The Kinematics and Dynamics of the Globular Clusters and the Planetary Nebulae of NGC 5128*, *Astron.J.* **134** (2007) 494–510, [[arXiv:0704.1189](#)].
- [101] S. Samurovic, *Dynamical constant mass-to-light ratio models of NGC 5128*, *Astron. Astrophys.* **514** (2010).
- [102] P. Goudfrooij, J. Mack, M. Kissler-Patig, G. Meylan, and D. Minniti, *Kinematics, ages, and metallicities of star clusters in ngc 1316: a 3 gyr old merger remnant*, *Mon.Not.Roy.Astron.Soc.* **322** (2001) 643, [[astro-ph/0010275](#)].
- [103] J. Scharwaechter, P. McGregor, M. Dopita, and T. Beck, *Kinematics and Excitation of the Molecular Hydrogen Accretion Disc in NGC 1275*, [arXiv:1211.6750](#).
- [104] R. Catena and P. Ullio, *A novel determination of the local dark matter density*, *JCAP* **1008** (2010) 004, [[arXiv:0907.0018](#)].
- [105] J. Geehan, M. A. Fardal, A. Babul, and P. Guhathakurta, *Investigating the Andromeda Stream. 1. Simple analytic bulge-disk-halo model for M31*, *Mon.Not.Roy.Astron.Soc.* **366** (2006) 996–1011, [[astro-ph/0501240](#)].
- [106] K. Bekki and S. Stanimirovic, *The lost dark matter in the SMC*, [arXiv:0807.2102](#).
- [107] Y. Sofue, Y. Tutui, M. Honma, A. Tomita, T. Takamiya, *et. al.*, *Central rotation curves of spiral galaxies*, [astro-ph/9905056](#).